5-2019

DEVELOPMENT OF AN UWB RADAR SYSTEM

Matthew Abraham Richardson
University of Tennessee

To the Graduate Council:

I am submitting herewith a thesis written by Matthew Abraham Richardson entitled "DEVELOPMENT OF AN UWB RADAR SYSTEM." I have examined the final electronic copy of this thesis for form and content and recommend that it be accepted in partial fulfillment of the requirements for the degree of Master of Science, with a major in Electrical Engineering.

Aly E. Fathy, Major Professor

We have read this thesis and recommend its acceptance:

Benjamin J. Blalock, Garrett Rose

Accepted for the Council:

Dixie L. Thompson

Vice Provost and Dean of the Graduate School

(Original signatures are on file with official student records.)

DEVELOPMENT OF AN UWB RADAR SYSTEM USING DIRECT SAMPLING TECHNIQUES FOR SUBSURFACE DETECTION

A Thesis Presented for the
Master of Science
Degree
The University of Tennessee, Knoxville

Matthew Abraham Richardson
May 2019

DEDICATION

To Indira, Quinn,

John and Barbara

ACKNOWLEDGMENTS

ABSTRACT

An ultra-wideband radar system is built at the University of Tennessee with the goal to develop a ground penetrating radar (GPR). The radar is required to transmit and receive a very narrow pulse signal in the time domain. The bistatic radar transmits a pulse through an ultrawide spiral antenna and receives the pulse by a similar antenna. Direct sampling is used to improve the performance of the impulse radar allowing up to 1.5 GHz of bandwidth to be used for signal processing and target detection with high resolution. Using direct sampling offers a less complex system design than traditional lower sample rate, super-heterodyne systems using continuous wave or step frequency methods while offering faster results than conventional equivalent time sampling techniques that require multiple data sets and significant post-processing. These two points are particularly important for a system that may be used in the field in potentially dangerous environments. Direct sampling radar systems, while still frequency limited, are continually improving their upper frequencies boundaries due to more power efficient, higher sampling rate analog to digital converters (ADCs) which relates directly to better sub-surface resolution for potential target detection.

TABLE OF CONTENTS

LIST OF TABLES

LIST OF FIGURES

ABBREVIATIONS AND SYMBOLS

FCC   Federal Communications Commission

UWB   Ultra-Wideband

ADC   Analog to Digital Convertor

FFT   Fast Fourier Transform

PRI   Pulse Repetition Interval

PRF   Pulse Repetition Frequency

RMS   Root Mean Square

LSB   Least Significant Bit

PSD   Power Spectral Density

GPR   Ground Penetrating Radar

ETS   Equivalent Time Sampling

RF   Radio Frequency

ISI   Inter-Symbol Interference

DS   Direct Sampling

CHAPTER 1:

INTRODUCTION AND GENERAL INFORMATION

Ground penetrating radar (GPR) is a relatively new technology in the field of radar which can detect both metallic and non-metallic objects alike using electromagnetic signals. These systems can perform sub-surface scans without the need to physically disturb the environment by obtaining information on the variation of the electromagnetic properties of permittivity and conductivity. With high speed signal processing, large areas can be rapidly measured and analyzed to provide detailed localized 3D-images of subsurface features. The challenge of this technology is to be able to provide a portable, practical and affordable system that can produce reliable detection results [1]- [9].

It is the goal of this research to develop a system that is suitable for these tasks in the applications of target data collection, precision location and tracking. The selection of system components must be carefully considered. Frequency and bandwidth dictate the resolution of the subsurface radar system. As bandwidth and frequency are increased, better resolution is obtained at the expense of the depth of penetration. As a result, designs are a compromise between these parameters. Table 1-1 summarizes these considerations in overall system design.

In the following work, we will progress through the development of a bistatic direct sampling impulse radar system that is compact with ultra-wide bandwidth, good impedance matching, circular polarization, and unidirectional radiation pattern.

Table 1-1 Summary of Performance Factors [10]

System Parameter	Affected Performance	Result of Parameter Variation
Frequency	Lateral resolution Penetration	Higher = Better Lower = Better
Bandwidth	Depth resolution	Higher = Better
Power	Depth penetration Signal to Noise (SNR)	Higher = Better Higher = Better
Polarization	Clutter Suppression	Depends antenna location (at or above surface)
Beamwidth	Lateral resolution	Larger = Better

This work is divided into chapters that focus on the critical subsystems as well as the complete radar system. Chapter 2 details the RF direct sampling ADC and focuses on the merits of direct sampling as well as a comparison to super-heterodyne receivers. Chapter 3 provides details on the design of a custom ultra-wideband circularly polarized antenna in which a comparison to other antennas is made with specific application to subsurface radars. Chapter 4 compares this work to other ground penetrating radar systems. It also describes in detail the overall impulse radar system, inclusive of those key subsystems described in Chapters 2 and 3 and discusses the radar system features that determine signal resolution and detection. Finally, Chapter 5 summarizes the performance of this work and provides insight into future system development.

CHAPTER 2:

DIRECT SAMPLING ADCs

2.1 Introduction

The motivation to develop a system using radio frequency (RF) direct sampling comes about because of continuing advances in the field of high speed digital sampling. As sample rates have increased and the associated cost in power and real estate have diminished, the opportunity to use alternatives to heterodyne receiver architectures has become more compelling. Moreover, it will be shown in Chapter 4 that the need for wide bandwidth is critical in determining the minimum depth that a subsurface radar system can resolve a target. The higher the bandwidth, the closer to the surface a point of interest can be resolved unambiguously.

There are alternatives to using high speed RF ADCs that are discussed here. A popular technique that allows the use of much lower sampling rate ADCs is that of equivalent time sampling (ETS). While this technique is effective in producing very high equivalent sampling rates, the price that must be paid is ultimately in the number of synchronized iterations (frames) of data that must be captured to render the equivalent data. During this time, the scene under investigation must remain static. For mobile radar systems (drone or vehicle based) or in potential hostile situations, this becomes an impractical requirement and was therefore removed from consideration for this work.

This chapter explores the current state of the art in ADCs and concludes with the performance of the device selected for the 1.25 GHz direct sampling impulse radar system.

2.2 Background and Classification

ADCs can be grouped into three major categories as precision, high-speed and general-purpose devices. A somewhat arbitrary cut-off between the groups exists that involves the bit resolution and speed of the conversion. Converters with 8-14-bit resolution and conversion rates below 10 mega-samples/s are typically considered general-purpose while those with conversion rates greater than 10 mega-sample/s are considered high-speed. This leaves the precision category to be defined as those parts with 16 bits or more of resolution [11].

Further classification can be accomplished by grouping parts by their architecture. The majority of which fall under the following categories: flash, pipelined, successive approximation register, and sigma-delta. Each of these architectures offer certain advantages to accuracy, speed of conversion or other parameters and this architecture determines the suitability for a given application.

ADCs have been implemented both as discrete and integrated circuit monolithic designs. The monolithic development of ADCs has been greatly influenced by innovations in both the high-end processes such as bipolar, biCMOS, and SiGe, as well as the more mainstream CMOS processes [11].

As ADC designs have migrated to CMOS processes with smaller geometries, an increased possibility for performance enhancements and higher levels of integration are possible. This includes an increased number of conversion

channels on a single die or pulling on-chip the conversion related functions. Die size and package depend on the semiconductor process which drives the supply voltage, conversion speed and influences power dissipation [11].

2.3 Performance and Theory of Operation

In general, there are three universal parameters of merit for ADCs. These are sampling rate, resolution and power dissipation that when combined form two figures-of-merit, *P* and *F* which are defined as follows:

$$P = 2^B \cdot f_s \tag{2.1}$$

$$F = \frac{2^B \cdot f_s}{P_{diss}} \tag{2.2}$$

P being a figure for resolution and speed and F the ratio of P to power dissipation. In addition, to the above mentioned parameters, there is also system noise to be considered in the form of thermal noise, quantization noise [12] and aperture-jitter noise [13].

2.4 ADC Noise Sources

The amount of noise that is produced by the ADC is of great importance as it affects the overall fidelity of the digital version of the radar signal. The following sections detail the types of noise created by digitization of an analog signal.

2.4.1 Thermal Noise

The relationship of the sampling frequency to thermal noise has a 1 b/6 dBs/s relationship when at the Nyquist sampling rate for a given signal. However, when the capacitance noise from the sample and hold input stage of an ADC shows strong capacitive characteristics, it usually dominates the thermal noise. As such,

the capacitance noise (modeled as *kT/C* noise [14], where *k* is Boltzmann's constant, *T* is the Kelvin temperature, and *C* is the capacitance) is the input noise floor.

2.4.2 Aperture Jitter Noise

An external clock is typically used to generate ADC sampling times. Because of limits in clock accuracy and sample and hold circuit imperfections, unavoidable variations in clock timing occur. While the average interval between clock pulses is constant, there are still variations in instantaneous spacing between samples which is referred to as aperture jitter. This jitter causes errors in the timing of a sampled signal, degrades the noise floor of the ADC, and increases inter-symbol-interference (ISI). Furthermore, aperture jitter is directly proportional to the input signal's slew rate. The maximum aperture jitter is determined by the frequency and resolution of the ADC by

$$\tau_a = \frac{1}{2^N \cdot \pi \cdot f_{max}} \tag{2.3}$$

where *N* is the number of bits, f_{max} is the maximum frequency and τ_a is the aperture jitter [12]. The distortion by aperture jitter can be modeled as another noise source. [15] provides an equation of signal to aperture jitter noise ratio (SANR) versus sampling rate

$$\text{SANR} = -20 \log_{10}(2\pi \cdot f_s \cdot \tau_a) \text{ dB}, \tag{2.4}$$

where f_s is the sampling frequency.

SNDR is the sum of all three noise sources which can also be represented as ENOB [12].

$$ENOB = (SNDR - 1.763)/6.02 \tag{2.5}$$

Resolution and signal quality are related in [16] and can be used for calculating an equivalent resolution by looking just at SANR. As such, the number of bits, B, can be represent as

$$B = -3.322 \log_{10}(f_s) - 3.322 \log_{10}(\tau_a) - 2.945 \tag{2.6}$$

which has a 1 b/3.322 dBs/s slope for aperture jitter τ_a.

2.4.3 Quantitation Noise

The amplitudes of analog signals are quantized into a binary word of fixed length, usually between 6 and 18 bits. The process of quantization is inherently nonlinear and is seen as wideband noise which limits an ADC's dynamic range. The expression for quantization noise is

$$SNR_{A/D} = 10 \log_{10}(\frac{signal\ variance}{quantization\ noise\ variance})$$

$$= 10 \log_{10}(\frac{\sigma_{signal}^2}{\sigma_{A/D\ noise}^2}) \tag{2.7}$$

If a uniform probability for quantization error is assumed, the denominator of Eq. 2.7 can be rewritten as

$$\sigma_{A/D\ noise}^2 = \frac{V_p^2}{3 * 2^{2b}} \tag{2.8}$$

Further, if loading factor LF is defined as

$$L_F = \frac{input\ signal_{rms}}{V_p} = \frac{\sigma_{signal}}{V_p} \tag{2.9}$$

And noting that variance σ^2 is a power expression and the standard deviation a root mean square (RMS) value, the square of the loading factor can be rearranged to obtain the following:

$$\sigma^2_{signal} = (LF)^2 V_p^2 \qquad (2.10)$$

Substituting Eqs. (2.8) and (2.10) into Eq. (2.7), yields

$$SNR_Q = 6.02N + 4.77 + 20\log_{10}(L_F) \, dB \qquad (2.11)$$

L_F is the loading factor, a measure of analog input voltage level. The parameter is defined as the analog input root-mean-square (RMS) voltage divided by the ADC's peak input voltage. When a sinusoid with an amplitude equal to the ADCs full-scale range is applied to the input, L_F becomes 0.707. As such, the last term in the SNR_Q equation becomes −3 dB and the ADC's maximum output signal-to-noise ratio is

$$SNR_{Q-max} = 6.02N + 4.77 - 3 = 6.02N + 1.77dB \qquad (2.12)$$

For this work, 12 or 14-bit resolutions were used, resulting in a maximum output-signal-to-noise ratio of 74.01 dB and 86.05 dB respectively.

SNR_{Q-max} leads to the 6 dB/b rule of thumb for the SNR of an ADC. This is, however an optimistic rule since it is based on an ideal ADC. It should also be noted that the input amplitude rarely equals the full-scale range exactly, which also increases the loading factor term in Eq. (2.11) [17].

2.4.3.1 Methods for reducing quantization error

Assuming the 6 dB/b for ADC SNR as previously shown, oversampling is considered as an approach to improve the SNR_Q. An analog signal is digitized at an f_s sample rate that is higher than the minimum rate needed to satisfy the Nyquist criterion and then lowpass filtered. Quantization noise power is the squared value of the converter's least-significant-bit (LSB) voltage divided by 12:

$$\text{Total quantization noise power} = \sigma^2 = (LSB\ value)/12 \qquad (2.13)$$

Oversampling assumes that the quantization noise is truly random and has a flat spectrum in the frequency domain. It should be noted, however that this assumption only holds for large signal amplitudes (close to the full-scale range of the ADC) that are not highly periodic [17].

Another aspect of quantization noise is its power spectral density (PSD) which is measured in power per Hz. With PSD, quantization noise can be represented as a certain amount of power per unit bandwidth. The random noise assumption results in a fixed value based on the converter's LSB voltage and the amplitude of this quantization noise PSD. PSD is the total quantization noise power divided by the total bandwidth f_s over which it is present:

$$PSD_{noise} = \frac{2}{12} > \left(\frac{1}{f_s}\right) = \frac{(LSB\ value)^2}{12 f_s}\ W/Hz \qquad (2.14)$$

If the LSB value in the numerator is reduced by using an ADC with additional bit resolution, the PSD_{noise} is likewise reduced.

Dithering is another technique used to minimize the effects of ADC quantization noise and is a method in which noise is added to the analog signal prior to ADC conversion. Dithering results in a noisy analog signal that crosses additional converter LSB boundaries and yields a quantization noise that is much more random, with a reduced level of undesirable spectral harmonics. Dithering raises the average spectral noise floor but increases SNR. Dithering forces the quantization noise to lose its coherence with the original input signal, which benefits from averaging, if desired [17].

2.4.4 Performance vs Power Dissipation

A derivation of power dissipation of an ideal ADC is presented in [18] and finds its basis on the assumptions that power is consumed only at the sample and hold block and the input signal supplies the power to charge the sample and hold capacitance.

Quantization noise should be no larger than the thermal noise dominated by sample and hold capacitance within the required bandwidth, a structure- and substrate-independent relationship between minimal power, P_{min}, sampling rate, and resolution is:

$$P_{min} = k \cdot T \cdot f_s \cdot 10^{\frac{(6N+1.76)}{10}} W, \qquad (2.15)$$

where k is the Boltzmann's constant and T is temperature, respectively. This is as derived in [19] and can be rewritten as

$$\log_{10}(P_{\min}) = \log_{10}(f_s) + \frac{6N}{10} + \log_{10}(k \cdot T) + 0.176 \qquad (2.16)$$

2.5 Application in RF Receivers

Direct-sampling (DS) radio frequency (RF) receiver architectures are becoming increasingly practical as an alternative to the heterodyne receiver architecture. Both architectures have a similar lower bound on power dissipation, which can be progressively approached as the ratio of process to the maximum signal frequency increases [20].

2.5.1 Comparison of Direct Conversion to Super Heterodyne RF receivers

The argument is that simultaneous requirements for sensitivity and blocker tolerance in a radio receiver require an adequate combination of converter

resolution and sample rate. The RF ADCs require a much higher sampling rate than baseband ADCs in a conventional receiver. Oversampling gain permits significantly lower resolution, which balances the power dissipation [20].

In a direct-sampling receiver, channel selection is implemented using digital mixers and filters after the ADC. The noise in each channel is the noise density of the ADC integrated over the bandwidth *B* of the channel selection filter— approximately the same as the channel bandwidth. If this is less than the ADC Nyquist bandwidth, the receiver benefits from oversampling gain OSR = 10log10(*fs*/2) − *B*. Given specifications of the receiver full scale and noise figure, we can ideally trade ADC effective resolution ($ENOB_{SNR}$) for ADC sample rate (*fs*) [20].

2.5.1.1 Impact of Linearity and PLL Phase Noise

Phase noise and nonlinearity constitute significant challenges to direct-sampling RF implementation. However, these noise sources are similar to analog heterodyne transceivers noise.

DS receiver phase noise was analyzed in [21]. It concluded that the ADC clock phase noise and the LO phase noise were about the same. That is, that ADC sampling and mixer commutation have comparable effects on signal fidelity. [20]

2.5.1.2 Power Requirements for Digital Down Conversion

RF direct-sampling output data must be digitally channelized. In one implementation the channelizer(s) are digital downconverters and filters or alternatively as an FFT. The high data rate and precision of the output points toward potentially significant power dissipation in the process of digital down

conversion. In [20] the argument is made that the power dedicated to digital down conversion will not dominate the power dissipation budget for direct-sampling RF.

2.5.1.3 Direct Sampling vs. Heterodyne: Recent Results

Reference [22] presents an agile conventional heterodyne receiver for software-defined radio (SDR) for carrier frequencies spanning 0.4–6 GHz. The power dissipation of these receiver designs ranges roughly from 35 to 100 mW, not including the synthesizer. Reference [23] presents a power dissipation of these synthesizer designs that range from 25 to 60 mW. Combining these values, we infer that a reasonable approximation for power dissipation of contemporary receivers (including PLL) is 60–160 mW and reference [24] presents a complete multiband cellular transceiver. It reports receiver power dissipation, including the synthesizer, bearing out this estimate. These values clearly show comparable power consumption. Likewise, [20] draws a comparison between the intrinsic SNR-limited dynamic range, showing the heterodyne to RFDS systems to be within 10 dBFs/Hz of each other.

2.6 Device Selection

Two major venders working in the RF direct sampling space are considered; Texas Instruments and Analog Devices. While both companies offer several different options for potential selection, the dual channel 3 GSPS pipeline ADCs offered by Texas Instruments fit most closely to the intended radar application in this work. The criteria includes the number of ports, bit resolution, sampling frequency and dynamic range given the 1.25 GHz upper frequency limit of the system.

Since the original ADC selection in 2017, both companies have produced additional chips that exceed the current ADC32RF45 part specifications. This shows the continued interest and momentum of the industry in this area of deign.

2.6.1 High Level Specifications

Two modules are needed to acquire high speed signal data using the offerings from TI. The ADC32RF45 connects to the TSW14J56 using a JESD204B communication pipeline for high-speed data transfer. Data passes from the ADC32RF45 to the TSW14J56 where it is stored in on-board memory. The memory contents are then able to be accessed via a USB 3.0 interface from the TSW14J56. Table 2-1 is a summary of the performance specifications for the ADC. Figure 2–1 shows the two modules connected.

2.6.2 ADC32RF45 Detailed Specifications

Figure 2–2 shows the internal block diagram of the ADC32RF45. Some of the key features include the input buffer which is designed with on-chip terminations

Table 2-1 ADC Gross Performance Characteristics

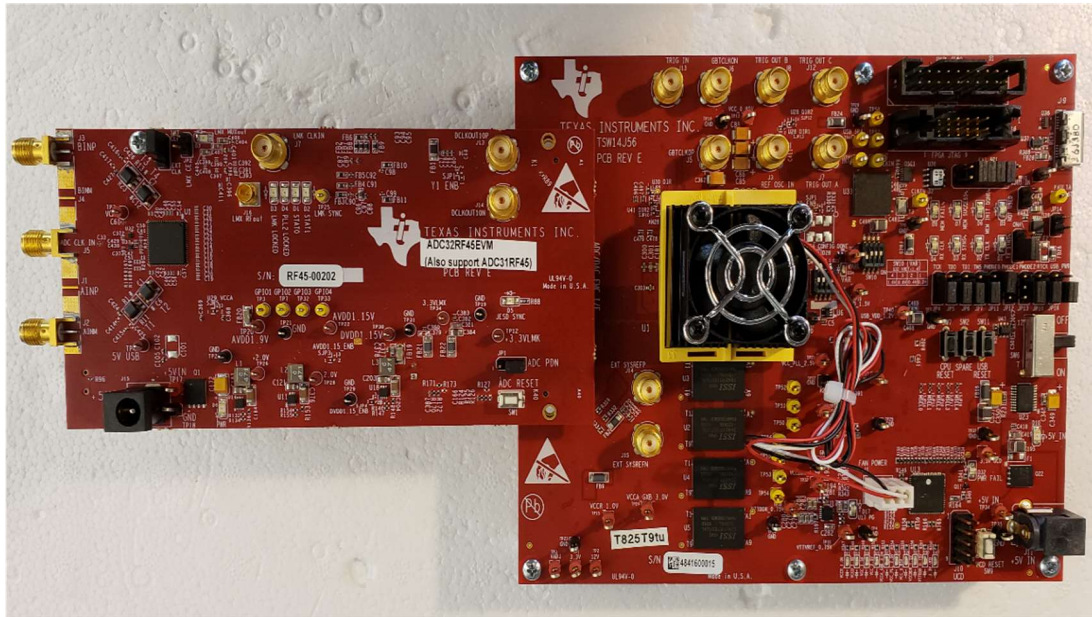| Parameter	Value
Number of Bit	14 b
Number of Channels	2
Sample Rate	3 GS/s
Aperture Jitter	90 fs
Channel Isolation	95 dB @ 1.8 GHz
Analog Bandwidth	3.2 GHz
SNR @ 2.5 GS/s	~60 dBFs

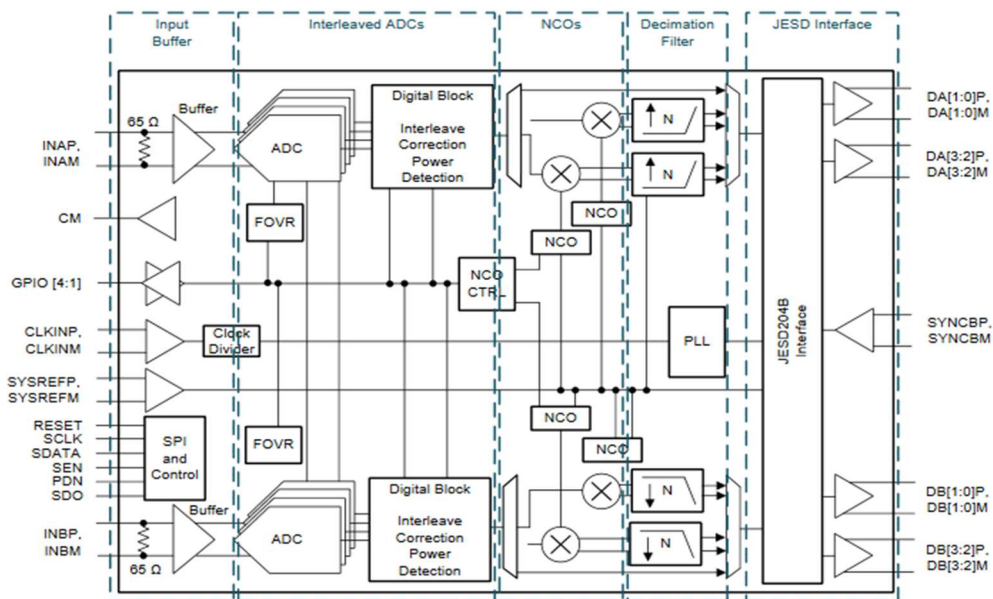*Figure 2–1 TI ADC32RF45 (left) and TSW14J56 (right)*

Figure 2–2 ADC32RF45 Functional Block Diagram

to provide uniform impedance across the analog bandwidth and to minimize sample-and-hold glitch energy. Two 14-bit, 3-GSPS ADC channels are provided as a 4x interleaved structure. The channels include analog and digital background, interleaving correction. In addition, 3 independent, complex 16-bit numerically controlled oscillators (NCO)s are included per ADC for frequency tuning within the Nyquist zone prior to digital filtering. The module also has a decimation filter to artificially decrease the sample rate by removing samples from the data stream to keep data rates reasonable for transmission. Processed data is then passed to the JESD204B interface, where the data is encoded, framed and serialized on one to 4 lanes per channel depending on sampling rate and decimation. The interleaved ADCs first sample the RF signal then the NCO shifts the frequency, followed by decimation and finally data transport. It should be noted that during the interleaving process, non-linearities create undesired harmonic and interleaving spurs. Figure 2–3(d) shows the interleaving noise contribution vs frequency.

Figure 2–3(a) through Figure 2–3(d) are provided by the manufacturer datasheet and are included for reference. In Figure 2–3(a) we note that as the signal amplitude increases, the SNR drops at values greater than ~-30 dBFs.

2.7 Validation of Device Specifications

Device operation is validated using a 200 mV, 1 GHz sinusoid which is equivalent to the ADC full-scale range value of -16.6 dBFs. The drive level is selected based on Figure 2–3(a), which is approximately the maximum input drive level before SNR and SFDR begins to degrade. The sine wave is generated from an Agilent E4421B signal generator. The ADC32RF45 is configured using the
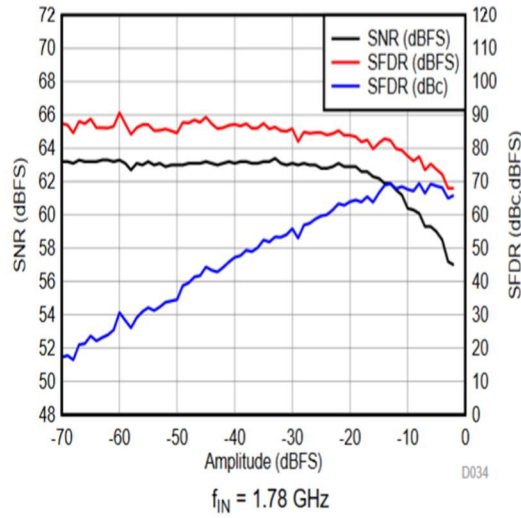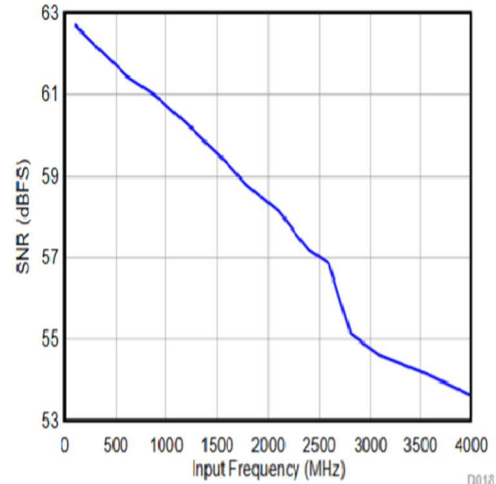
13
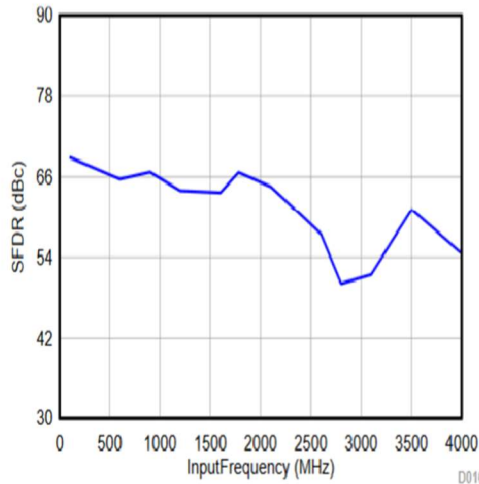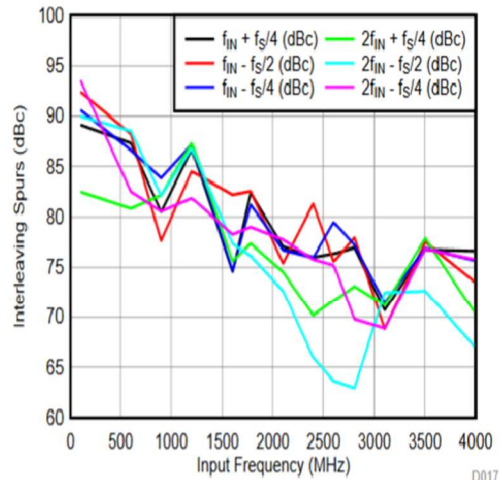
Figure 2–3 (a) Performance vs. Amplitude, (b) Signal-to-Noise Ratio vs Input Frequency, (c) Spurious-Free Dynamic Range vs Input Frequency, (d) Interleaving Spur vs Input Frequency

LMX2582 wideband RF PLL synthesizer found on the ADC module, with a 12-bit sampling resolution and sampling rate of 2.94912 GS/s. While the ADC is capable of 14-bit measurements, the 12-bit values were selected as worse case. The signal is then captured by the ADC32RF45 ADC and converted to the frequency domain for comparison. A total of 524,288 samples are used to construct a 1.474 GHz span, which produces an equivalent resolution bandwidth of 5.6 KHz. Table 2-2 provides the additional calculated performance of the ADC for the 1 GHz reference signal shown in Figure 2–4 and Figure 2–5.

Table 2-2 ADC32RF45 Specifications

Attribute	Value
SNR	55.35 dBFs
SFDR	77.83 dBFs
ENOB	8.90 bits
THD	79.50 dBFs
Next Spur	-77.83 dBFs

It should be noted that the value obtained was measured at ~-17.5 dBFs (~180 mV) which is slightly less than the 200 mV signal under investigation. This difference is attributed to the cable losses from the signal generator to the measuring ADC. To support the previous measurement, the signal is also captured on an Agilent E4407B spectrum analyzer referenced in Figure 2–5.
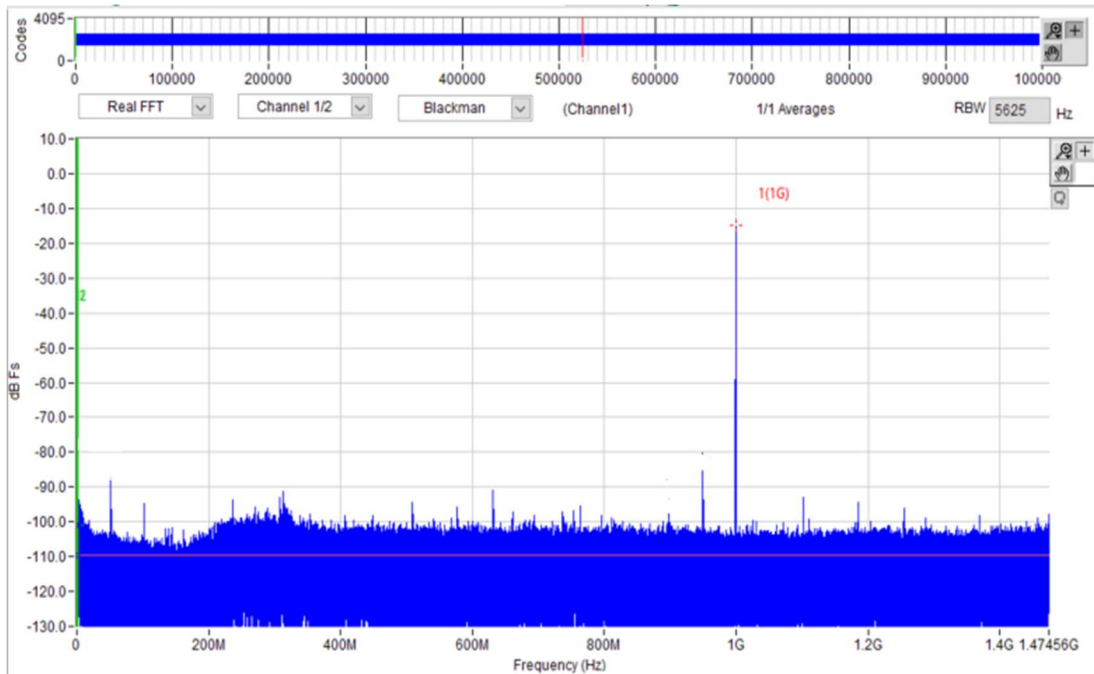
Figure 2–4 Captured 1 GHz Test Reference
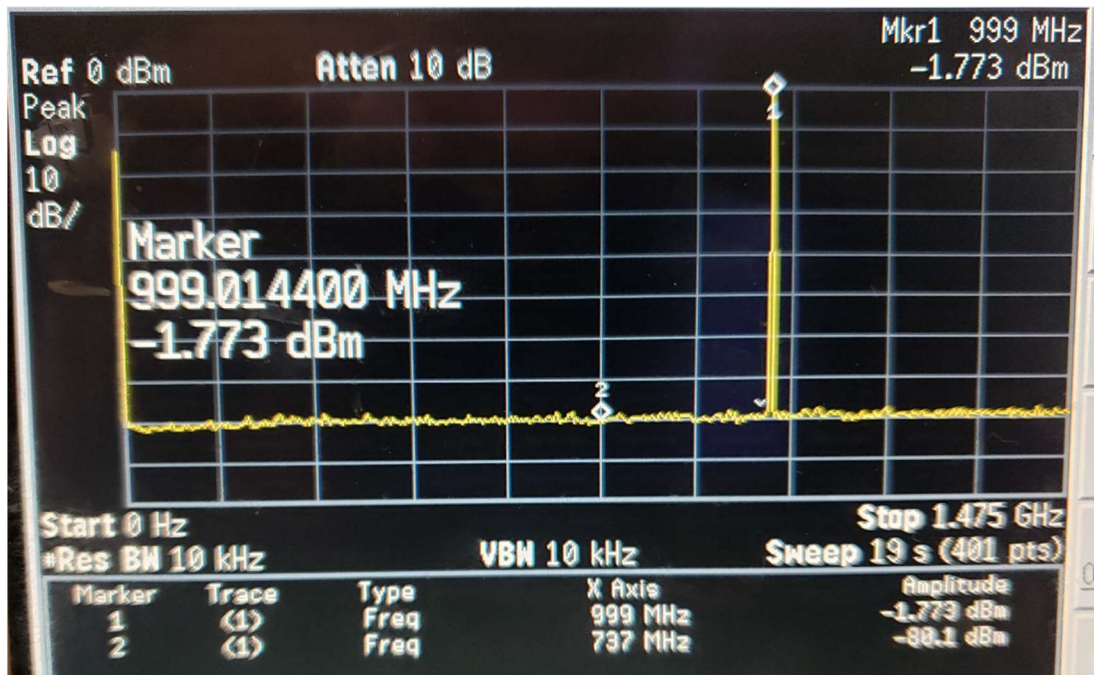
Figure 2–5 1 GHz Test Reference on Spectrum Analyzer

16

Comparing the results of the ADC to the spectrum analyzer reveals that the 1 GHz signal amplitude is -1.773 dBm, which is equivalent to 182 mV in a 50 Ohm system. Clearly the measurements obtained are equivalent.

2.8 Conclusion

The Texas Instruments ADC32RF45 exhibits excellent performance characteristics including analog bandwidth, sampling rate, SNR, and meets or exceeds the needs for the intended radar system.

CHAPTER 3:

ULTRA-WIDEBAND ANTENNAS

3.1 Introduction

Antenna selection is vital in the design and performance of UWB systems. The bandwidth, gain, polarization, radiation pattern, nondispersive group delay, system portability and regulatory constraints are all important parameters to consider [25] [26].

Table 3-1 shows frequencies commonly used for ultra-wideband imaging radar antennas in the range of 10 MHz to 10 GHz.

Table 3-1 GPR Frequency Selection

Frequency Range (GHz)	Application
0.01-2	Archeology and architecture
0.5-3	Military
1-10	Medical

3.2 Ultra-Wideband Antenna Structures

UWB Antennas are classified into six major groups: helical, frequency-independent, log periodic, horns, those derived from resonant antennas and arrays. Most can be designed as either 3D or planar structures [27]. As will be shown in Section 3.4, the antenna selected for use in the radar system is from the frequency independent group.

3.2.1 Basic Structures

The following, while not exhaustive, are widely used antenna structures for UWB applications.

Figure 3–1 shows examples of dipole antennas: **a** fat dipole; **b** bow-tie; **c** and **d** planar rectangular dipoles; **e** diamond dipole; **f** elliptical dipole; **g** and **h** biconical antennas with equal and unequal cone angles

Figure 3–2 shows examples of bow-tie antennas: **a** basic bow-tie; **b** rounded bow-tie; **c** bow-tie with resistive loading at the far end; **d** bow-tie with sections coupled through resistances.

Figure 3–3 shows examples of end-fire tapered slot antennas: **a** linearly tapered slot antenna; **b** exponentially tapered slot antenna, also called Vivaldi.

Figure 3–4 shows examples of three dimensional structures: **a** conventional horn; **b** TEM horn.

Figure 3–5 shows examples of spiral antennas: **a** self-complimentary 2-arms Archimedean spiral; **b** self-complimentary 4-arm Archimedean spiral; **c** equiangular or logarithmic spiral.

3.3 Frequency-independent Antennas

Frequency-independent antennas are based on Rumsey's Principle [28], according to which, an antenna whose geometry is solely defined by angles is frequency independent: the geometry is maintained at different scales which are determined by the operating wavelength. Thus, for increased frequency the geometry decreases and for decreased frequency the geometry increases for the antenna design.
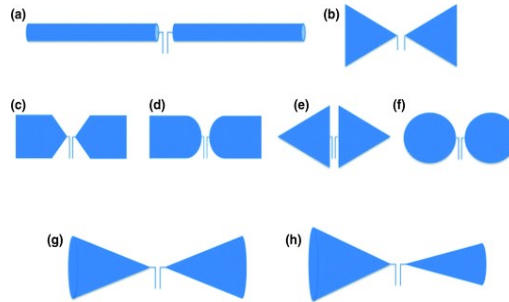
Figure 3–1 Example of Dipole Antennas
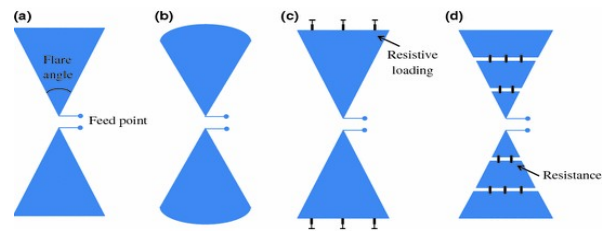
Figure 3–2 Example of Bow-Tie Antennas
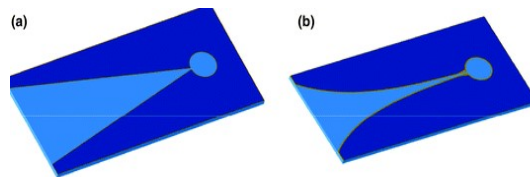
Figure 3–3 Examples of Slot Antennas
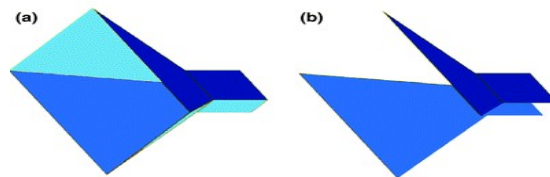
Figure 3–4 Examples of Horn Antennas
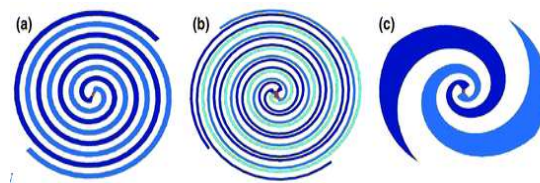
Figure 3–5 Examples of Spiral Antennas

20

A self-scaling antenna structure satisfies the following requirements [28]:

- The antenna contains its own scale model parts—continuous or discrete—that can be scaled to an infinitesimal size.

- The antenna radiates most of the power in a finite active region so that it can be terminated with minimal effect.

- Fed from the high-frequency end, the antenna must be a transmission line to carry power to the low-frequency end.

- The dimensions of the active region must scale with wavelength.

- The antenna must not radiate in the direction of expanding structure.

- The parts must have significant direct coupling outside the transmission-line feeder.

Some additional properties of antennas that follow the construction guidelines above, also express the following performance characteristics [29]:

- Have broadband frequency operation due to the frequency independent nature of their design.

- Archimedean spiral antennas usually have two uniform-width and length arms that can be fed symmetrically or coaxially.

- Radiates circularly polarized waves.

- Have medium directivity.

- Have low front-to-back ratio.

- Create bidirectional radiation in which back radiation is usually suppressed by cavity-backed mounting.

21

- Theoretically infinitely sized structures that when truncated for practical fabrication, become frequency limited, especially at the low frequency end of the antenna bandwidth.

- Long pulse dispersion (ringing); which makes them unsuitable for impulse-radiating systems with time-domain processing.

3.4 Antenna Selection

A log spiral antenna was selected for the UWB antenna for the impulse radar. The following points were considered in the selection process.

3.4.1 Center Frequency

When imaging radar signals propagate through non-homogeneous material, the medium attenuates higher frequencies more than lower frequencies. This is particularly true for material with high water concentrations. As a result, antennas designed for deep penetration are physically larger (lower frequency) than those used for high-resolution systems [30]. In the case of a GPR impulse radar system, a compromise between the resolution and penetration depth must be made.

A simple guide for determining signal penetration depth is to use the following formula:

$$Log_e f = -0.95 Log_e z + 6.95 \text{ [31]},\qquad(3.1)$$

where f is the operating frequency in MHz and z is the required depth of investigation in meters. By selecting the desired penetration to be 1 meter, and using equation 3.1 above, the operating frequency of the proposed cavity-backed antenna is calculated to be 1 GHz.

3.4.2 Structure

When selecting a radar imaging system antenna, mechanical considerations must be made concerning design complexity, size, and ruggedness. Table 3-2 shows a comparison of these features. The spiral antenna is clearly the superior mechanical choice.

Table 3-2 UWB Mechanical Properties

Structure	Geometry	General Size	Complexity	Rugged
Cone	3D + Ground	Large	Medium	No
Disc	Planar	Small	Low	Yes
Bow-Tie	Wire	Medium	Medium	No
Vivaldi	Planar	Medium	Medium	Yes
Double Ridged Horn	3D	Large	High	No
Spiral	Planar	Small	Low	Yes

Continuing with the refinement of a suitable antenna selection are the radiation properties, which include the pattern, polarization, directionality and gain. Table 3-3 provides a summary for these characteristics.

In imaging and detection applications, circularly polarized antennas are preferred for many reasons. Linearly polarized antennas are dependent upon the relative orientation between the antenna and target for the magnitude of the returned signal. Moreover, if the transmitting and receiving signals are perpendicular (cross polarized) to each other, there will be a severe reduction in power coupling between the two linearly polarized antennas. This reduction in

23

Table 3-3 Radiation Properties [29]

Structure	Radiation	Polarization	Gain (dBi at GHz)			
			0.5	1	2	3
Cone	Omni	Linear	1.6	3.2	4.4	4.0
Disc	Omni	Linear	1.4	5.1	5.3	6.6
Bow-Tie	Bi-Direct	Linear	3.8	3.3	5.2	5.8
Vivaldi	Direct	Linear	3.0	5.8	7.0	7.7
Double Ridged Horn	Direct	Linear	6.6	10.3	10.3	11.9
Spiral	Bi-Direct	Circular	1.7	3.9	5.8	5.5

power will degrade the system efficiency and performance [32]. Thus, the receiver would not detect the reflected target signal. Circular polarization, however, does not suffer from this inconvenience. Compounding this issue is the situation when the antenna is not located at or in the same propagation environment as the target. In this case, since the permittivity of an arbitrary medium is often greater than air, the polarization sense of a reflected wave from the surface at the discontinuous boundary will be of the opposite polarization of the incident wave. Therefore, the circularly polarized antenna does not receive the reflected wave from the boundary interface and the only detectable signal is the reflected signal from the target beyond the surface interface. For these reasons, a circularly polarized antenna is desirable [33].

With directionality and polarization in mind, the best choices are narrowed to the Vivaldi, DRH and Spiral antennas. This leaves the gain as the deciding factor. However, as will be explained in the next section, the gain of the spiral can be

improved through the technique described to levels comparable to those of the DRH or Vivaldi while creating a unidirectional antenna pattern.

Based on this information and the intended use is a GPR system, the spiral antenna is the best choice for polarization and directionality.

3.4.3 Technique for Improving Directionality and Gain of a Spiral Antenna

Inherent in the spiral antenna design is the bidirectionality of the antenna radiation. By adding a reflecting cavity to the back of the antenna at one quarter wavelength from the center frequency of the antenna, a unidirectional radiation pattern is obtained. It should be noted that wideband cavity-backed antennas use either an absorber, in addition to the cavity, to avoid destructive interference between the reflected and forward waves [34], or an absorber ring at the outer perimeter of the cavity. For this work, a cavity without absorbing material is employed to reflect the backward radiation in-phase and constructively add to the forward radiated energy, which increases gain and addresses directionality. The antenna center frequency of 1 GHz was selected for this effect [33].

Of further note, to mitigate coupling from the radiating arms to the antenna feed in the cavity, a shielding tube was added to the outside of the balun.

3.4.4 Return Loss

Figure 3–6 and Figure 3–7 show the general return loss for the UWB antennas structures under consideration.

For the selection of a broadband antenna, it should be noted that all the antennas shown have good return loss at the 1 GHz center frequency of the

25
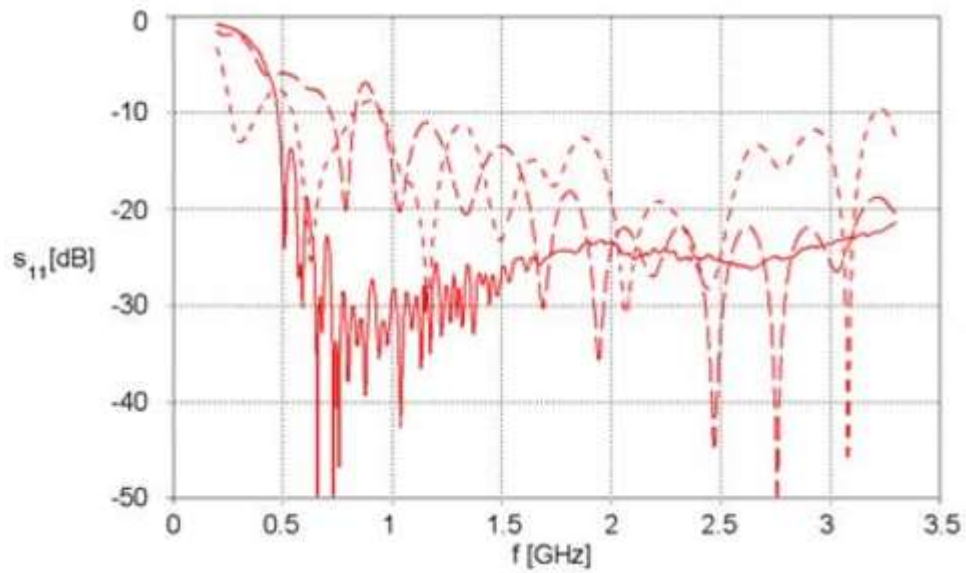
Figure 3–6 Return Loss for Spiral, DRH, Vivaldi
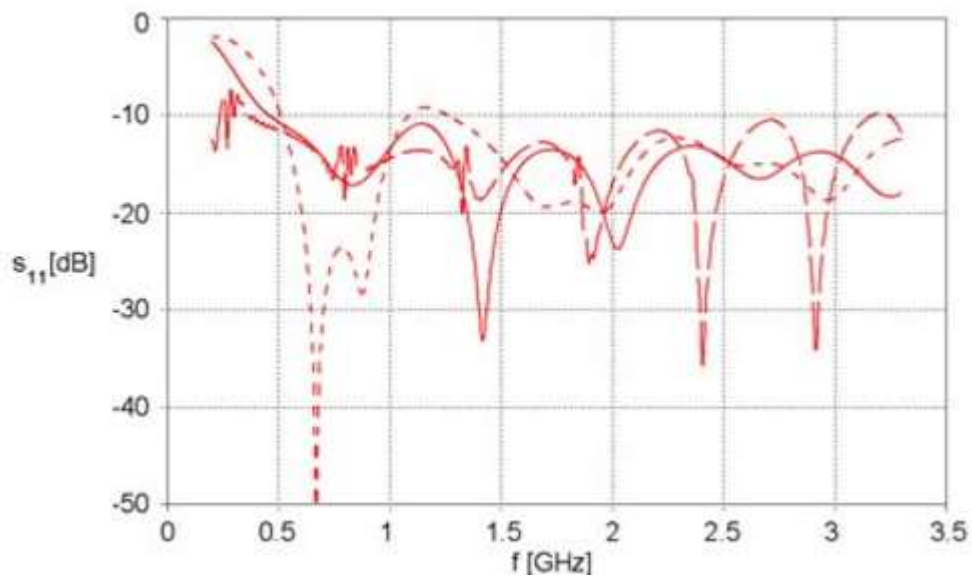
Figure 3–7 Return Loss for Cone, Bow-Tie and Disc Antennas

intended design. It is only when we approach the lower frequency range that this becomes an issue. The spiral can safely be used at 750 MHz and have better than 10 dB return loss and as such, is selected as the lower frequency cut off for the antenna. With the center of operation already determined to be 1 GHz, the overall bandwidth should be 500 MHz.

3.4.5 Dispersion

Like the previous section, this section provides two figures to show the characteristic dispersion created from the potential antennas.

The graphs of Figure 3–8 and Figure 3–9 show that the spiral antenna has dispersion and that it is not suitable for a time domain radar. The intended method for the radar system, however, is a frequency domain technique, making this a non-critical point.
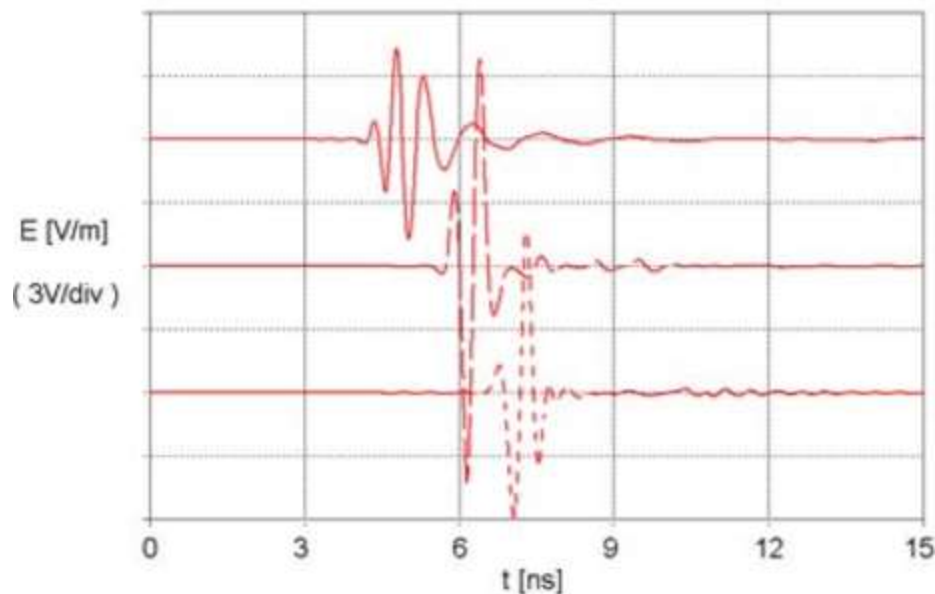
Figure 3–8 Spiral, DRH and Vivaldi Dispersion
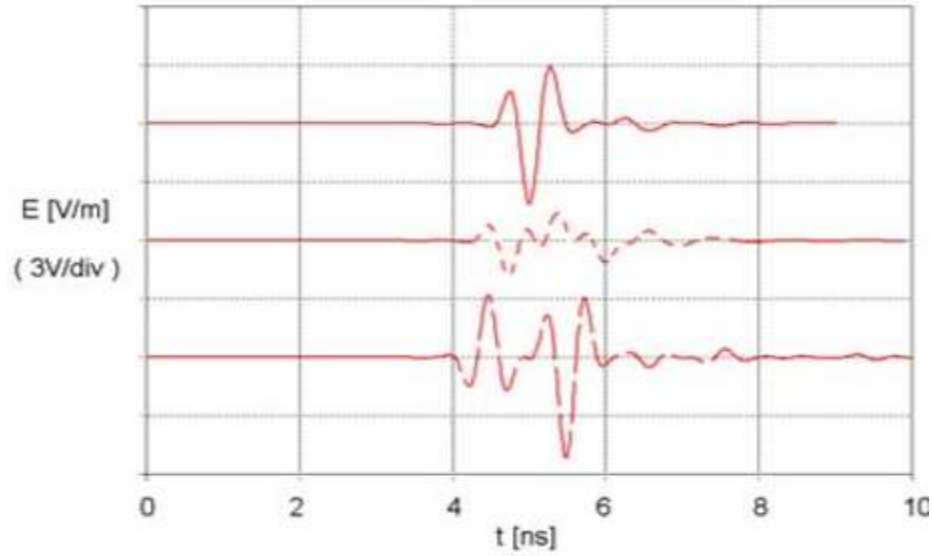
Figure 3–9 Cone, Bow-Tie and Disc Dispersion

3.4.6 Bandwidth

The last parameter to be considered is the bandwidth of the antenna. It will be shown in the next chapter that greater bandwidth provides better range resolution, so with all other factors considered, should be as large as possible. Thus, wideband antennas are needed, and ultra-wideband antennas are preferred.

3.5 Spiral Radiator Design

The spiral antenna is a self-complementary radiator [35] that when Mushiake's work is applied, yields an input impedance close to the theoretical value of $188\ \Omega$. A two-arm log-spiral that acts as a balanced antenna, is designed using the formulas of (3.8).

$$R_i = r_{in}e^{\alpha\phi}, \qquad R_o = r_{in}e^{\alpha(\phi-\phi_0)}$$

$$(3.8)$$

28

where R_i and R_o are the inner and outer spirals radii; r_{in} and $r_{in}e^{-\alpha\phi_0}$ are the initial inner and outer radii; α is the growth rate; ϕ_0 is the opening angle; and ϕ is the angular position. In [36], acceptable radiation patterns could be achieved with less than 1.5 turns of the spiral [33].

CST Microwave Studio is used to simulate the propagation and radiation characteristics of the antenna, including circular polarization, input impedance, and the radiation patterns. The following are the spiral construction variables used for the design: $\alpha = 0.22\ rad^{-1}, \phi_0 = 90°, r_{in} = 22\ mm$. The width and spacing between the arms are equal, and the antenna is a self-complementary spiral; meaning its characteristics are frequency-independent [36] [37]. Figure 3–10 shows the designed antenna with two equal arms and 1.7 turns. The arms are tapered at the end of the spirals, to improve matching with free space and a metal ring is added at the outer edge to widen the bandwidth.
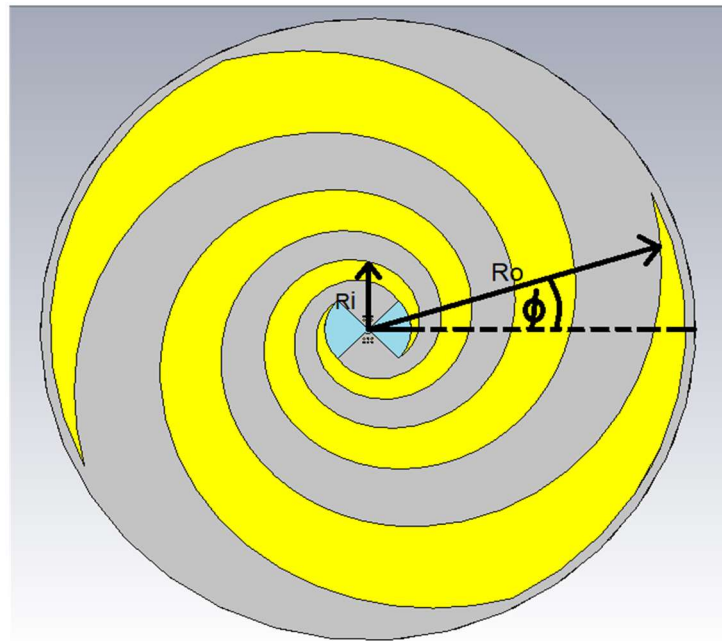
Figure 3–10 Spiral Antenna

As an additional improvement to bandwidth, a thick substrate with low permittivity is used to provide wider bandwidth and higher efficiency. Such gains come at the expense of greater size and are part of the trade-offs between size, simplicity, effectiveness and cost. The log-spiral antenna is designed on 10 mm foam substrate with ε_r of 1.03.

When the antenna is fed from its center, current radiates outward from the feed point to the outer edge of the arms. Its current density gradually decreases as this happens. Average current density at 1 GHz center frequency is shown in Figure 3–11, which illustrates bore axis symmetry and high current density distributed along the edges of the spiral arms.
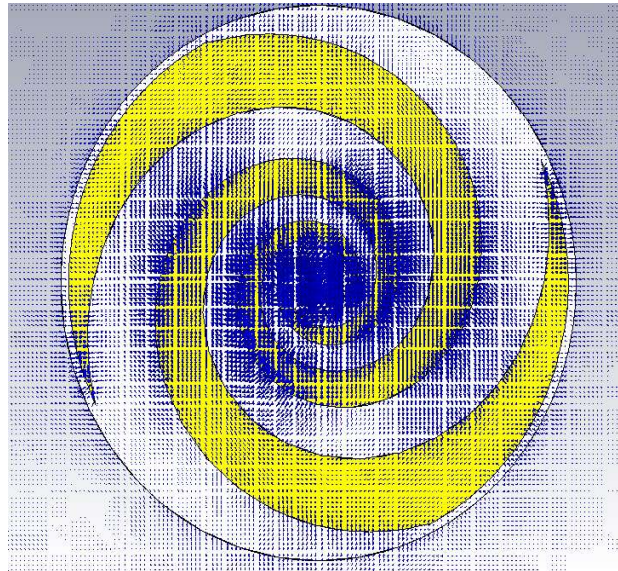
Figure 3–11 Spiral Antenna Current Density

Figure 3–12 shows the input impedance as a function of frequency for the antenna. A value of ~195 Ω is obtained from simulation of the spiral antenna.
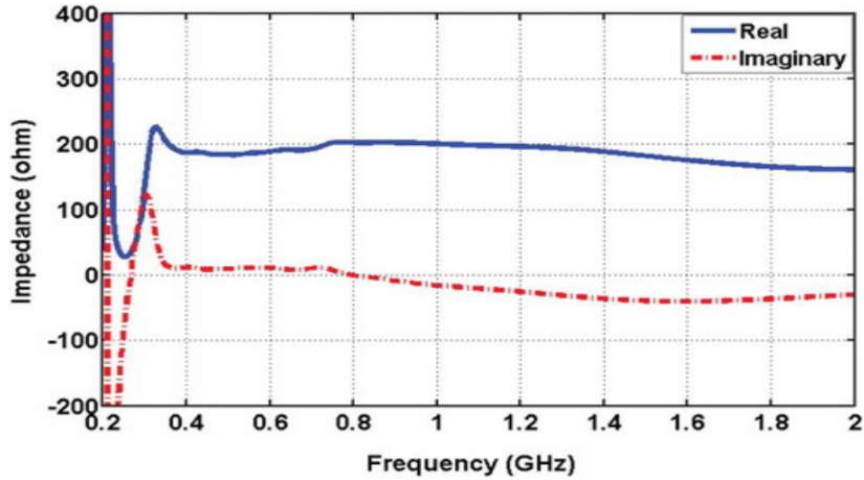
Figure 3–12 Simulated Antenna Input Impedance (Real and Imaginary)

3.6 Balun design

The balanced arms of the antenna structure require an impedance transformer/balun. A wideband balun is used to transition from the feed line microstrip to a parallel stripline at the center of the spiral antenna.

A quarter-wavelength impedance transformer is fabricated in which the impedance varies between the two boundary conditions of 50 Ω and 195 Ω. The balun/transformer, shown in Figure 3–13, has an exponentially tapered ground plane with a linearly tapered impedance transformer on top. The balun geometry is optimized for maximum bandwidth and minimum insertion loss. It is fabricated on FR4 substrate with the following specifications: 121 mm x 40 mm x 1.575 mm, $\varepsilon_r = 4.3$, and $\tan \delta = 0.027$. The balun is matched to a fixed 195 Ω resistive load for optimization. The results shown in Figure 3–14, indicate 10 dB or better return loss over the design bandwidth of 0.75 to 1.25 GHz.

31
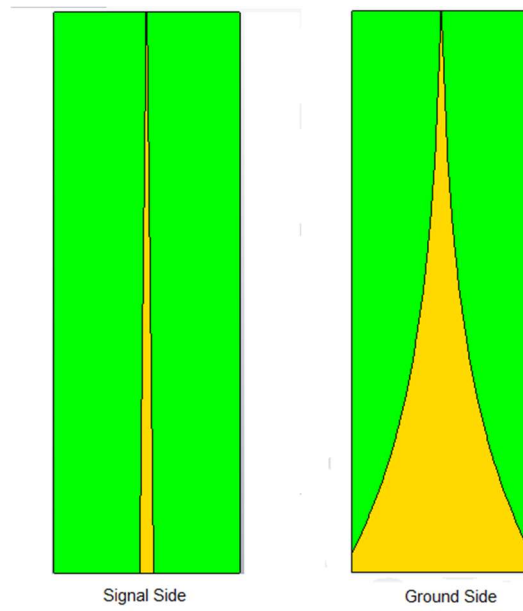
Figure 3–13 Ultra-Wideband Balun Design
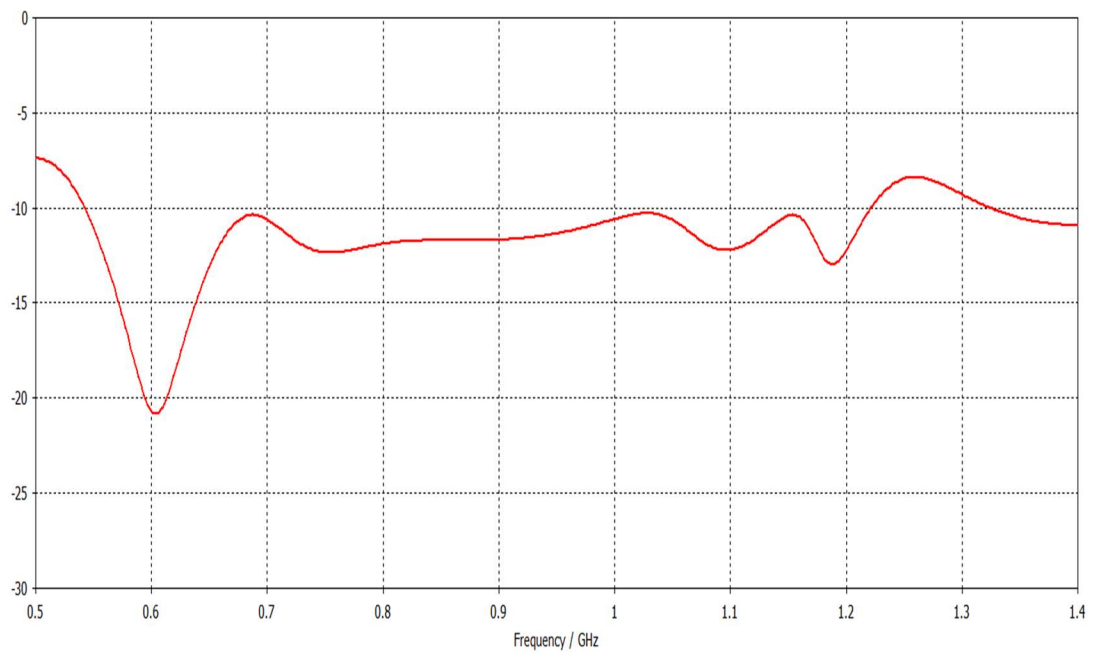
Figure 3–14 Antenna Return Loss

3.7 Logarithmic Spiral Antenna with Wideband Balun

As previously mentioned, impulse radar range and imaging systems require a radiation pattern from a single direction. A cavity is added to produce this desired effect on the spiral antenna. To increase gain and to prevent degradation of the antenna radiation performance, absorber material was not used. For the cavity to be effective, however, it must be equal to $\lambda/4$ in depth at the desired frequency to achieve constructive interference between the reflected backward and forward beams [38]. A diagram showing the cavity-backed spiral antenna and balun is shown in Figure 3–15. The 75 mm height of the cavity equals $\lambda/4$ at the bandwidth center frequency of 1 GHz. This value was obtained by recognizing that for constructive interference to occur, the wave must include a 180° phase shift through propagation, with another 180° phase shift from the cavity reflection. At 1 GHz the ¼ wavelength is 0.075 m.
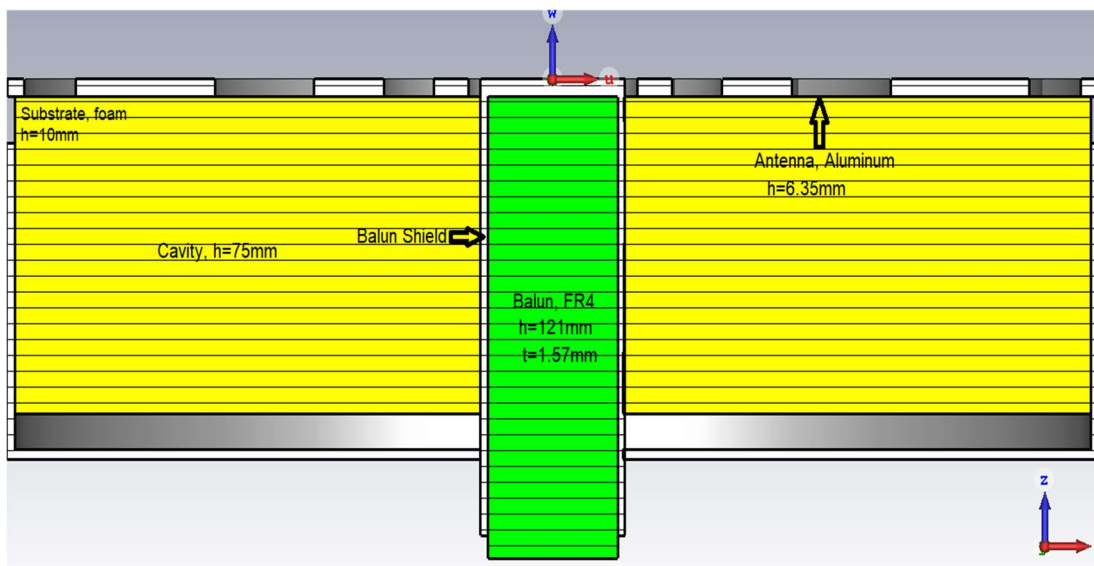
Figure 3–15 Spiral Antenna Cross Section with Cavity Back

3.8 Numerical and Experimental Results

The log-spiral antenna is manufactured on a foam substrate of 163.25 mm × 163.25 mm x 10 mm thickness with a permittivity (ε_r) 0f 1.03. Figure 3–16 illustrates the fabricated cavity-backed antenna and balun. A PVC tube is covered with copper foil and inserted into the cavity to improve overall performance by reducing coupled back radiation to the balun. Also, a 3-D printed plastic insert is added to facilitate a more robust method for mechanically holding the balun in place and joining the balun and the spiral antenna elements at the feed. The balun is fabricated on FR4 substrate and flexible wire extensions are used to connect to the antenna feed. The extensions improve the design as the original method of soldering the two rigid components together break often and easily. The antenna elements and back cavity are fabricated from aluminum. The antenna elements are 6.35 mm thick and the back cavity is 1 mm.
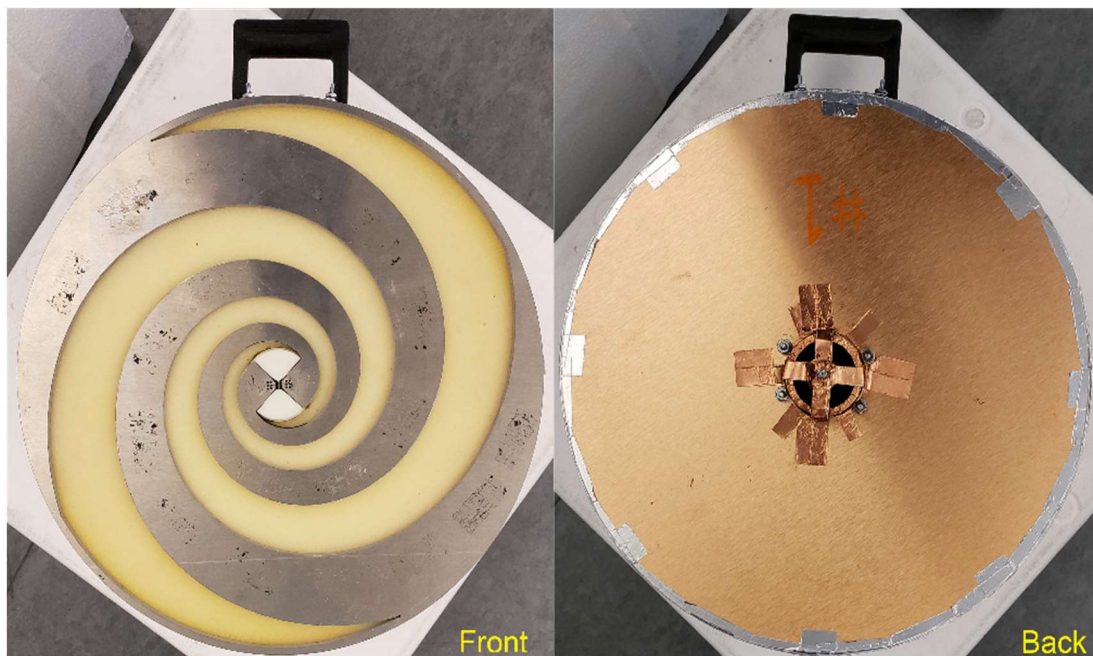
Figure 3–16 Front and Back of Fabricated Antenna

3.9 Frequency Domain Characteristics

An Agilent E8363B network analyzer is used to measure the reflection coefficients of the antenna. The simulation and measurement results are shown in Figure 3–17. The measured return loss impedance bandwidth is observed from 0.75 to 1.25 GHz to be greater than 10 dB (VSWR 1:2).
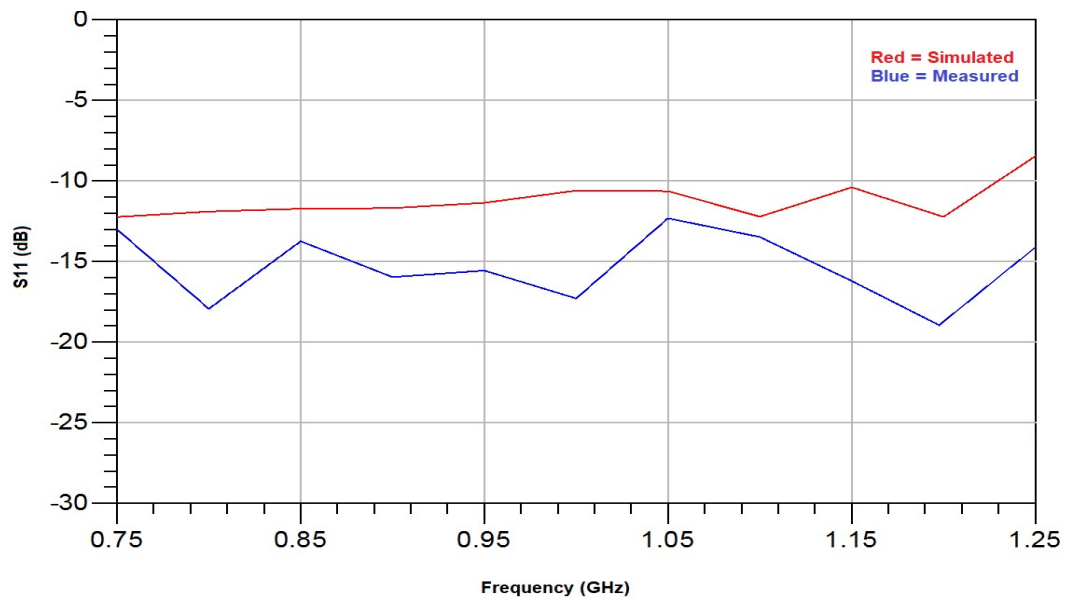
Figure 3–17 Measured and Simulated Antenna Reflection Coefficients

The measured and simulated radiation pattern results are illustrated in Figure 3–18. The radiation patterns and front to back ratio (~20 dB) are similar over the bandwidth. Furthermore, the maximum gain is compared in Figure 3–19, which ranges from 6 to 6.75 dBi over the band. Axial ratio is commonly used to determine circular polarization performance and should be less than 6 dB [39]. The axial ratio in Figure 3–20 shows an axial ratio in the boresight direction that is less than 4 dB within most of the band.
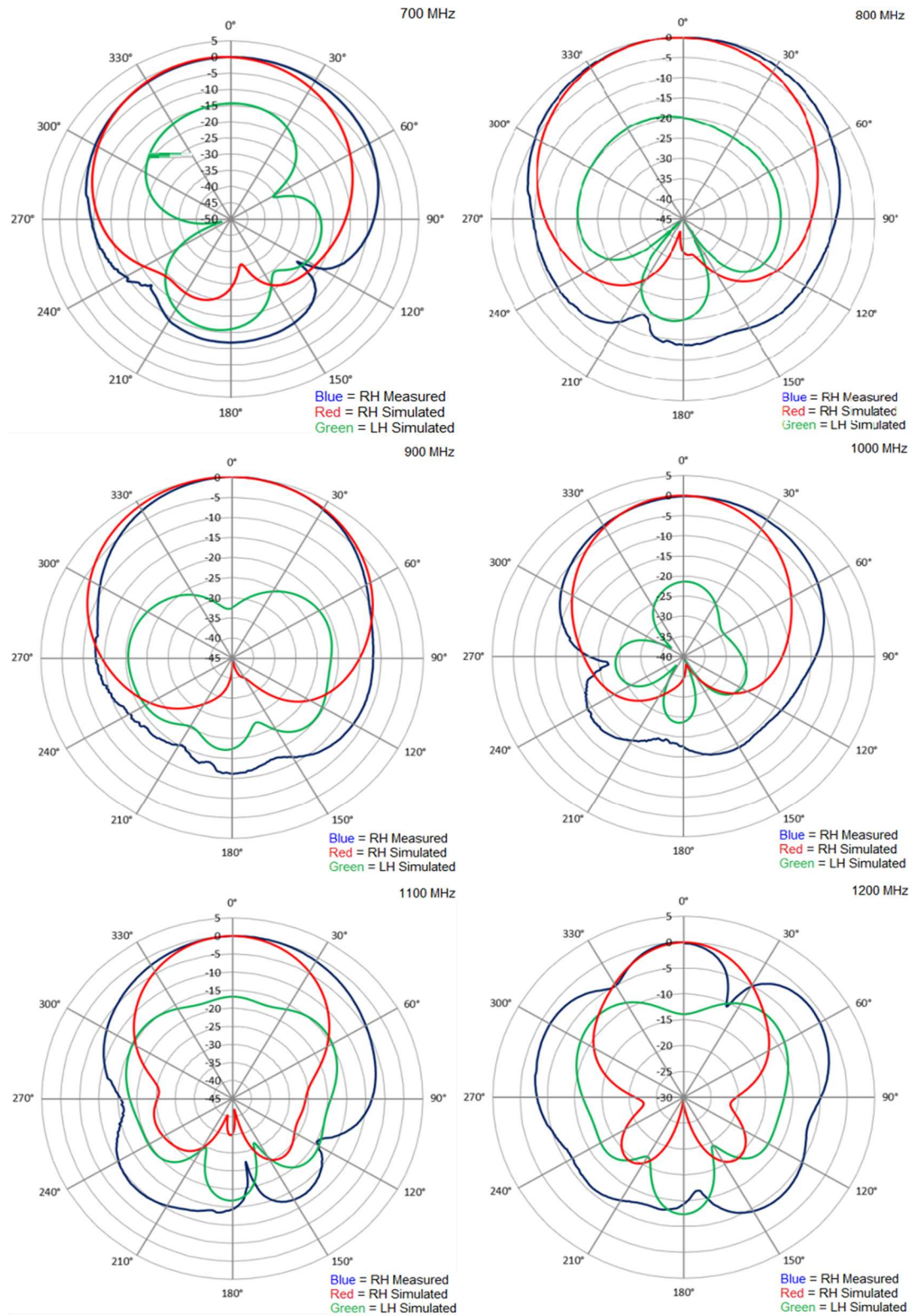
Figure 3–18 Selected Frequency Antenna Radiation Patterns

36
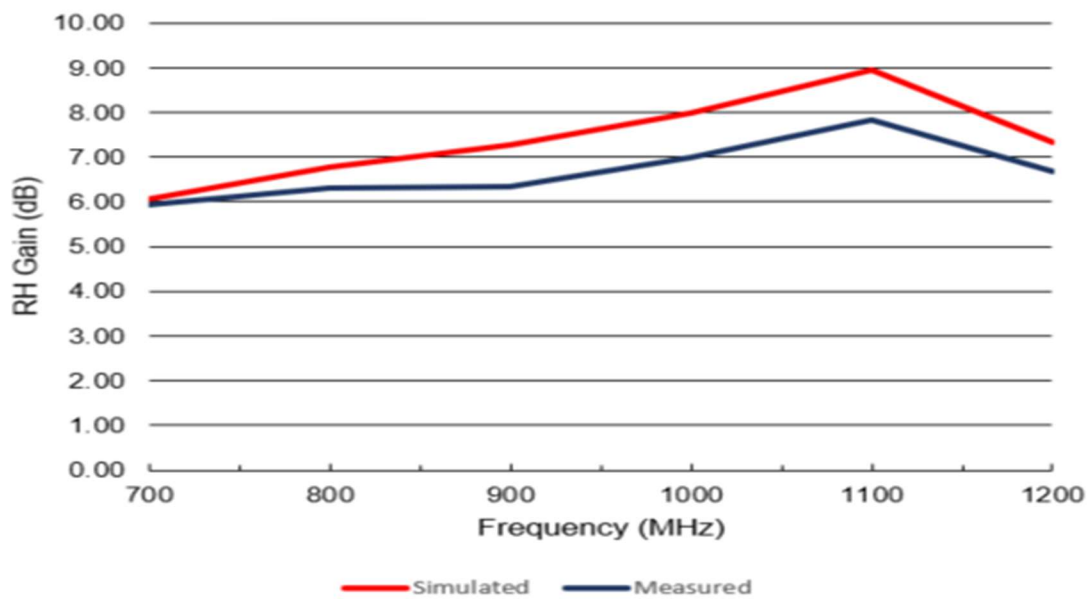
Figure 3–19 RHCP Gain vs Frequency Along Boresight (Theta = 0)
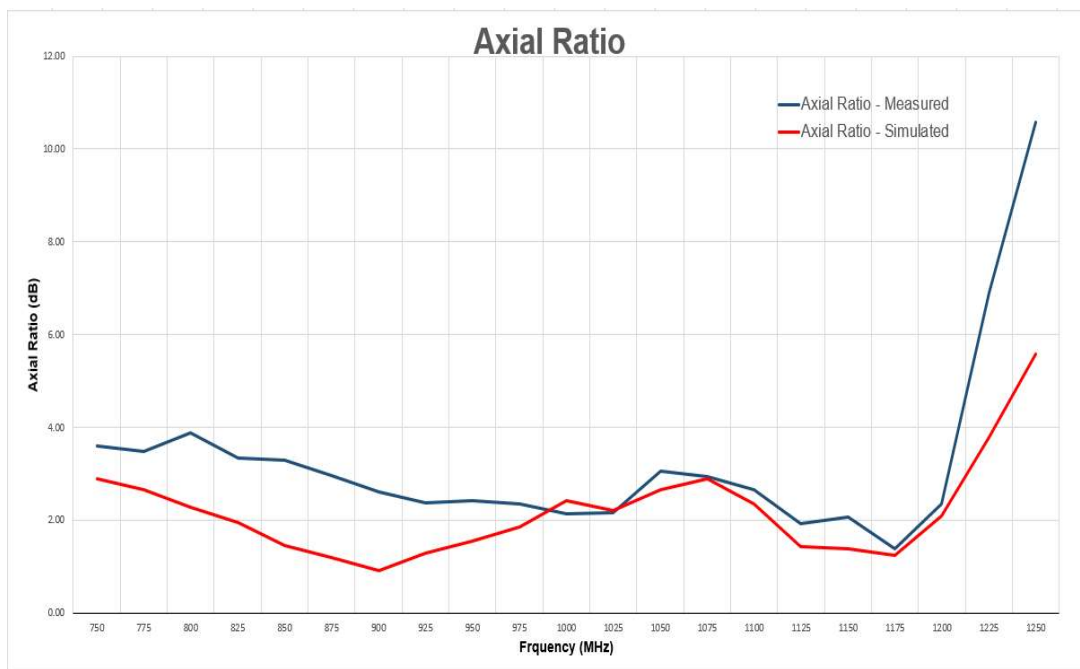
Figure 3–20 Antenna Axial Ratio

3.10 Transient characteristics evaluation

UWB Signal dispersion significantly affects time domain performance of transmitted pulses as it distorts the pulse and reduces the radar resolution [40]. Spiral antennas are, in general, dispersive antennas [41]. To evaluate the antenna, the dispersion characteristic is measured with a Gaussian pulse. The time domain pulses are shown in Figure 3–21 and Figure 3–22, which show antenna dispersion. The dispersion is caused by variations of the phase center location which is found in most spiral antenna structures.

Because impulse radar antennas require linear phase characteristics, it is a non-trivial task to avoid transmitted pulse distortion and reduced resolution [42] [43]. Nondispersive antennas should have constant group delay over the bandwidth. As shown in Figure 3–23, the group delay of the designed spiral antenna demonstrates a maximum variation of 11 ns within 0.5:1 bandwidth.

3.11 Conclusion

A logarithmic cavity-backed spiral antenna and wideband balun are presented for an ultra-wideband impulse radar. The antenna covers the frequency range from 0.75 to 1.25 GHz with better than 10 dB return loss (BW = 0.5:1). The bandwidth allows for penetration depth of 1 meter and provides moderate resolution of ~0.1 meter. In addition, the antenna has a low axial ratio (less than 4 dB for most of the band), wide bandwidth (> 500 MHz), and high gain (> 6 dBi) which are well suited characteristics for an imaging impulse radar.
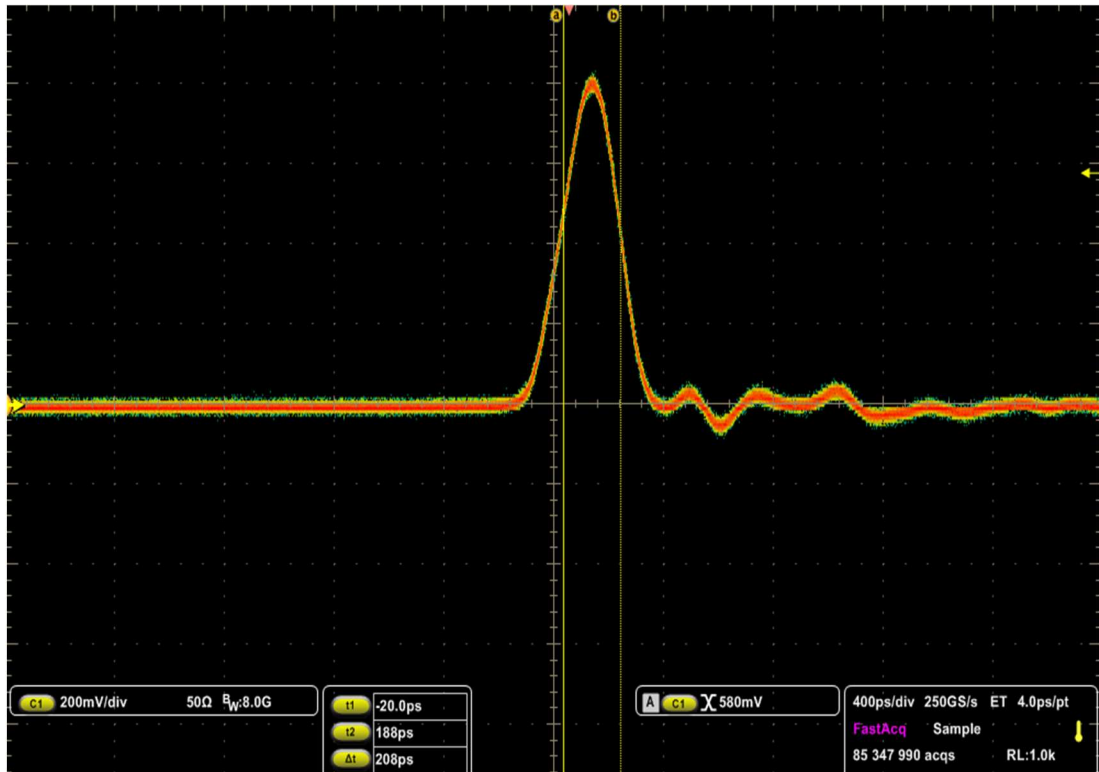
Figure 3–21 Time Domain, Transmitted Impulse
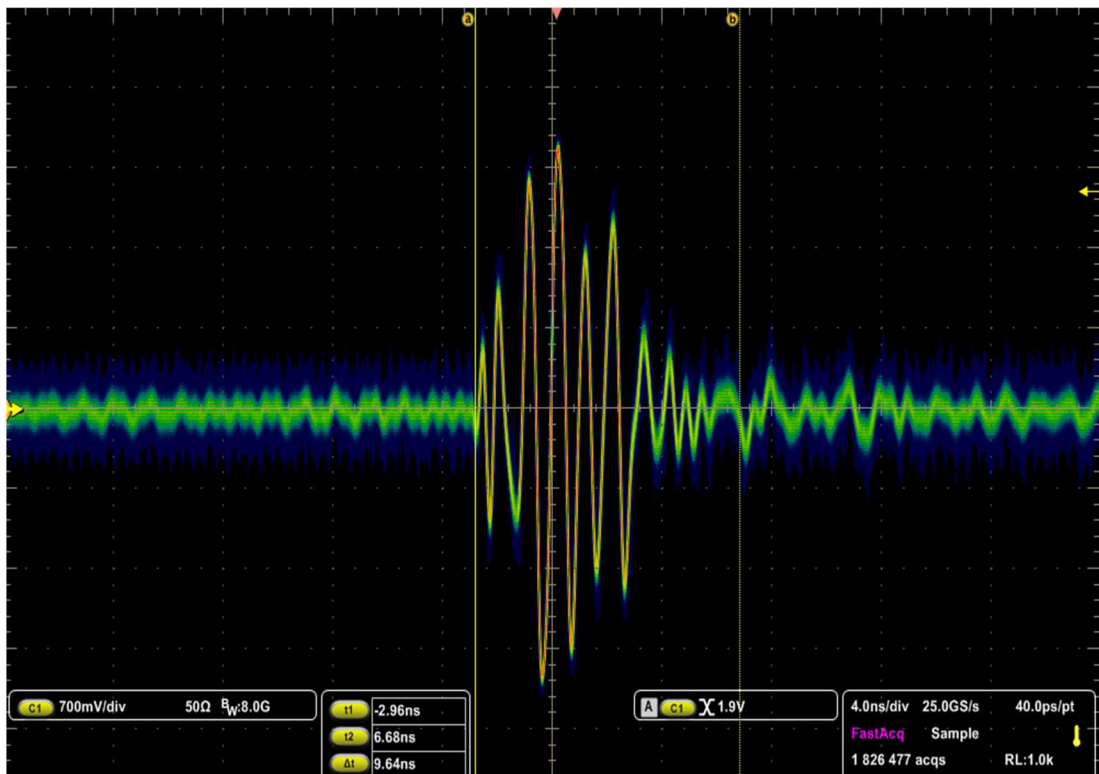
Figure 3–22 Time Domain, Received Pulse
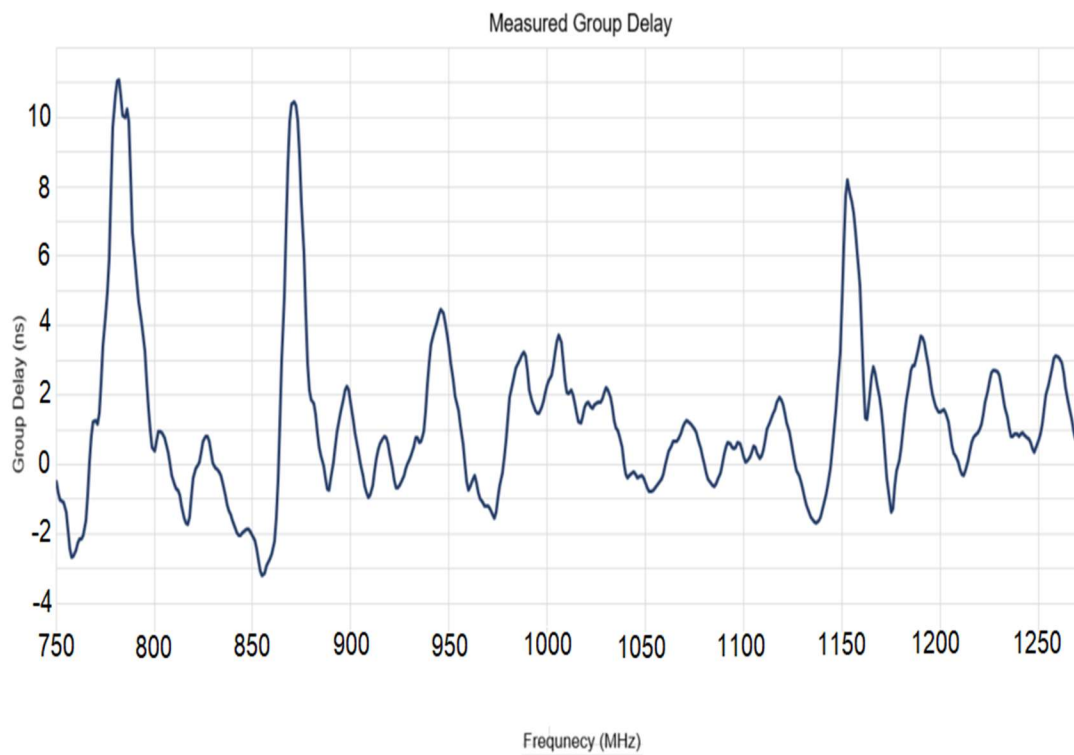
Figure 3–23 Group Delay

CHAPTER 4:

RADAR SYSTEMS

4.1 Introduction

Subsurface detection radar systems have several design parameters that are in direct opposition. Therefore, the design must be approached with care. Looking at the state of the art in GPR systems provides some historical insights into the choices that have been made in prior works. Table 4-1 provides the details of several GPR systems.

Table 4-1 State of the Art in GPR Systems

Radar Type	Frequency Range	Mono / Bistatic / Array	Antenna Type
Impulse [44]	1.2 GHz – 3.5 GHz	Monostatic	Double Ridge Horn
Short Pulse [45]	100 MHz – 1.3 GHz	Array (2x2)	TEM Horn
SFCW [46]	1 GHz – 2 GHz	Monostatic	Double Ridge Horn
SFCW + CS [47]	300 MHz – 3 GHz	Bistatic	Bow-Tie
Impulse [48]	600 MHz – 6 GHz	Bistatic	TEM Horn
SFCW [49]	8 GHZ – 12 GHz	Bistatic	Double Ridge Horn
Impulse - This work	750 MHz – 1.25 GHz	Bistatic	Spiral

The general factors that affect GPR performance include the frequency, bandwidth and pulse repetition frequency (PRF). Higher frequency radar systems have finer cross range resolution that scales with inverse proportionality to

frequency. However, as can be seen in Table 4-2, as frequency increases, so too does the attenuation of the signal. Bandwidth is also of extreme importance as it is inversely proportional to range resolution and PRT determines the maximum unambiguous range of the system.

Table 4-2 Material Loss at 0.1 and 1 GHz [50]

Material	Loss at 100 MHz (dB/m)	Loss at 1 GHz (dB/m)
Clay (moist)	5-300	50-3000
Loamy soil (moist)	1-60	10-600
Sand (dry)	0.01-2	0.1-20
Ice	0.1-5	1-50
Fresh Water	0.1	1
Sea Water	100	1000
Concrete (dry)	0.5-2.5	5-25
Brick	0.3-2	3-20

Most GPR designs are based on either time or frequency-domain signal processing techniques which dictate the transmitted type of signal used to illuminate the targets of interest. In general, for the time domain systems, there is either amplitude modulated (AM) or continuous wave (CW) systems and for the frequency domain options there are impulse radars (IR), stepped frequency continuous wave (SFCW), and frequency modulated continuous wave (FMCW) radars.

Continuous wave (CW) radars are band-limited signals and continuously transmit and receive sine waves. In this configuration, it is possible to detect buried targets, but it is not possible to resolve range information since the signals do not change. In addition, a common problem for CW is the strong backscattered signal from the air-ground interface. This undesired signal can overshadow the reflections from actual targets, especially those with low radar cross section, and limit the dynamic range of the receiver, which could be saturated and blocked.

With amplitude modulation, or pulsed radar, it is possible to acquire range data, however, this type of system lacks control of the power spectral density and in turn the resolution of the assessment.

An alternative to the time domain, single frequency approach is to add more transmitted frequency waveforms. This configuration is called FMCW. Instead of using transmitted and received times of pulses, FMCW uses the difference in frequency. This type of GPR system, however, suffers from interference issues.

Yet another frequency domain solution is to modify the CW or AM (pulsed) design by transmitting a frequency of tones or pulses which are then shifted in a given interval or steps across a defined bandwidth. In this way, the signal spectrum is finite and not continuous. This technique is called SFCW. The frequency step avoids phase ambiguity by measuring the phase difference between returned signals at each frequency. However, this method also suffers from interference susceptibility issues.

This clearly leaves the impulse radar system as the desired choice for the GPR. As mentioned above, the advantages and disadvantages of different waveforms

for GPR are also dependent upon operational requirements. One of the challenges when using impulse waveforms is that of producing a pulse short enough to achieve the desired bandwidth with suitably fast rise and fall times.

4.2 Pulse Radar Principles of Range and Resolution

Pulsed radars use a train of pulsed waveforms (mainly with modulation). In this category, radar systems can be classified based on the Pulse Repetition Frequency (PRF), as low PRF, medium PRF, and high PRF radars. Low PRF radars are primarily used for ranging where target velocity (Doppler shift) is not of interest. High PRF radars are mainly used to measure target velocity. Continuous wave as well as pulsed radars can measure both target range and radial velocity by utilizing different modulation schemes.

4.2.1 Range

A synchronous impulse radar uses a reference timing source, which is used throughout the system. Signals are generated on the timing sources clock edge and sent to the transmitting antenna. In similar fashion, the receiver amplifies the radar returned signals and prepares them for signal processing by the ADC. Target information is extracted by signal processing. The range, R, to the target is determined by the time delay, t; taken by the pulse to travel the two-way path between the target and the radar. Since the pulse, which is an electromagnetic wave, travels at the speed of light, $c = 3x10^8 \, m/s$, then

$$R = \frac{c\Delta t}{2} \qquad\qquad (4.1)$$

where the range, R, is in meters and Δt is in seconds. The factor of $\frac{1}{2}$ is used to account for the two-way time distance. For the impulse radar developed, this calculation was performed in MATLAB on a PC

A pulsed radar often will transmit a pulse train or burst of pulses, as shown by Figure 4–1. The Inter Pulse Period (IPP) or Pulse Repetition Interval (PRI) is associated by T, and pulse width by τ. The inverse of the PRI is the Pulse Repetition Frequency (PRF), which is denoted by f_r,

$$f_r = \frac{1}{PRI} = \frac{1}{T} \tag{4.2}$$
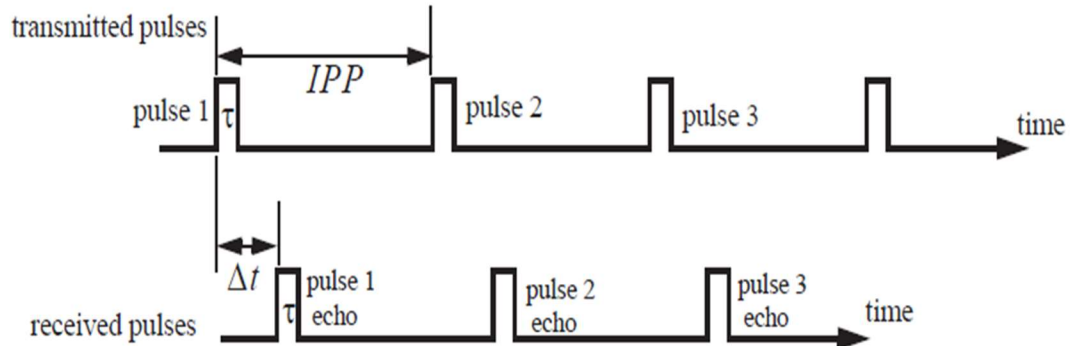
Figure 4–1 Train of Transmitted and Received Pulses [51]

Each PRI radiates energy for only τ seconds. The rest of the PRI is dedicated to listening for the returns from the target. The transmitting duty cycle (factor) d_t of the radar system is defined as the ratio $d_t = \tau/T$. Thus, the average power transmitted is

$$P_{av} = P_t \times d_t \tag{4.3}$$

where P_t is the peak transmitted power. The pulse energy, E_p, is

$$E_p = P_t \tau = P_{av} T = P_{av}/f_r. \tag{4.4}$$

R_u, the unambiguous range, is the distance traversed by the two-way time delay, T, of the signal. Figure 4–2 shows the return signal, Echo 1, from a target that is a distance $R_1 = ct/2$ away from the transmitter. Echo 2 is either the return from the same target due to pulse 2, or a return from a further target at range R_2 due to pulse 1. In this case,

$$R_u = \frac{ct}{2} \ \text{or} \ R_2 = \frac{c(T+t)}{2} \tag{4.5}$$
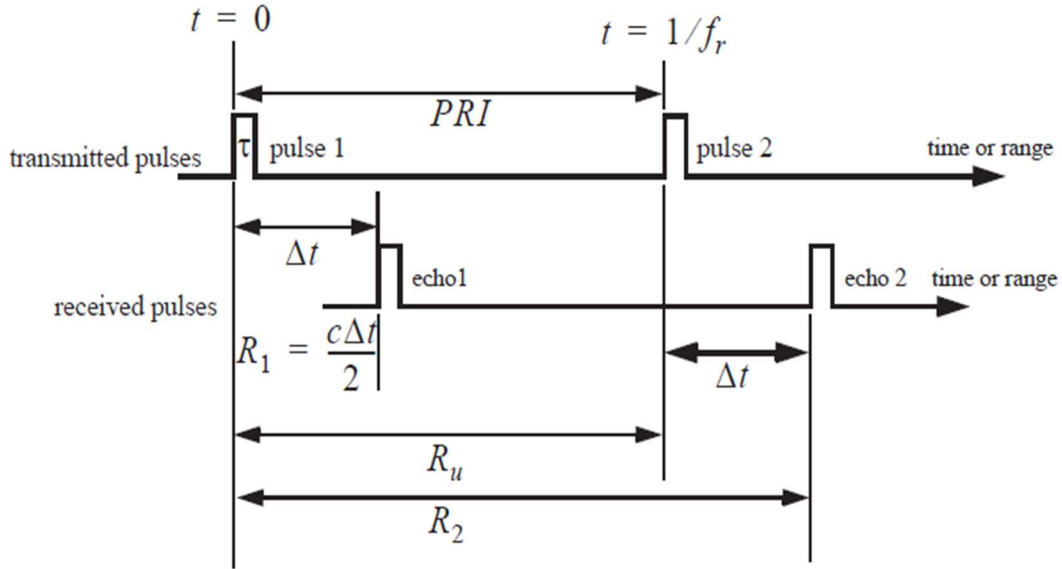
Figure 4–2 Range Ambiguity Illustration [51]

This clearly illustrates range ambiguity associated with echo 2. This forces the requirement that a radar must wait for a period of time so that returns from targets at maximum range are received before the next pulse can be emitted. Accordingly, the maximum unambiguous range correspond to half of the PRI,

46

$$R_u = \frac{cT}{2} = \frac{c}{2f_r} \qquad\qquad (4.6)$$

4.2.2 Range Resolution

ΔR denotes range resolution, a radar metric that describes the ability to distinctly resolve targets that are near each other. Design limitations force radar systems to operate between a minimum and maximum range denoted by R_{min} and R_{max}. When the distance between these two distances is divided into M range bins, of width ΔR we arrive at the following equation.

$$M = (R_{max} - R_{\min)}/\,\Delta R \qquad\qquad (4.7)$$

$$\Delta R = \frac{c\tau}{2} = \frac{c}{2BW} \qquad\qquad (4.8)$$

Where c is the speed of light, and BW is the radar bandwidth.

A target separated from another object of interest by at least ΔR can be completely resolved in range. Alternatively, a target within the same range bin that is unresolvable can still be identified in the cross range (azimuth) by using signal processing techniques.

In general, ΔR should be as small as possible to improve the radar performance. As suggested by Eq. (4.8), to achieve fine range resolution, one must minimize the pulse width which increases operating bandwidth and also reduces the average transmitted power.

4.3 UWB System Design

An ultra-wideband system is built using the key components of the RF direct sampling ADC and an UWB antenna discussed in Chapters 2 and 3. The system

developed is a direct sampled, ultra-wideband impulse radar. See Figure 4–3 for the system block diagram.
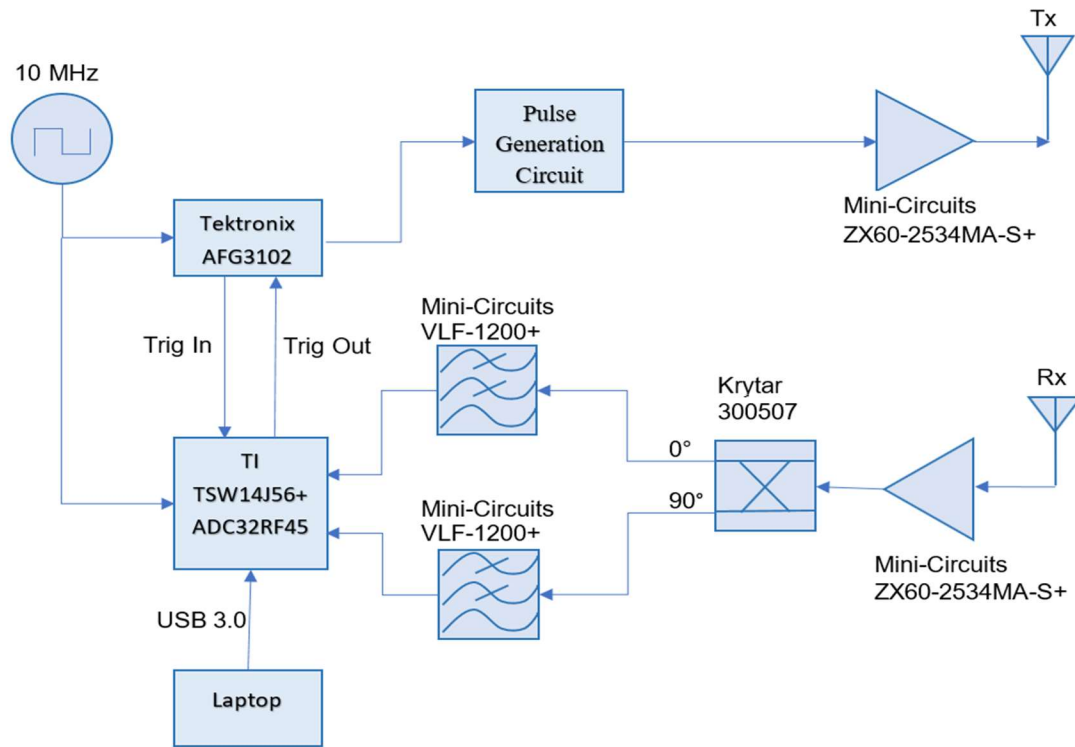
Figure 4–3 Impulse Radar System Block Diagram

The system uses the Tektronix AFG3102 signal generator to excite the pulse generation circuit. The pulse generated is ~200 ps and 800 mVp. The pulse circuit was developed by [52]. The schematic can be seen in Figure 4–4 and the output pulse can be seen in Figure 3–21. This signal is then amplified by the ZX60 broadband amplifier. The ZX60 is technically classified as an LNA, but the device was more than adequate for the output gain, given regulatory restrictions. It also ensures symmetrical performance between the Tx/Rx path. After the amplifier, the TX pulse passes though the transmitting antenna.
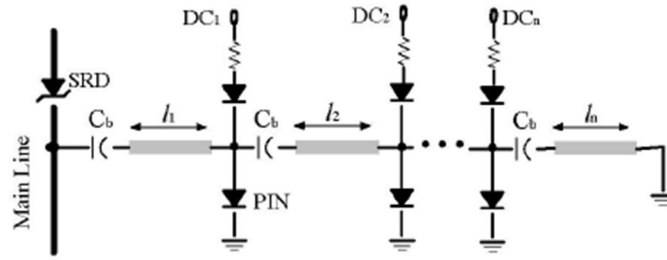
Figure 4–4 PIN Diode Pulse Circuit Schematic

One the RX side, a similar ZX60 amplifier is used to boost the incoming signal, which is then split using the Krytar quadrature hybrid. The signals then pass through anti-aliasing filters and are sampled by the ADC32RF45 RF ADCs. The raw magnitudes are stored and transferred to a PC using the Texas Instruments High Speed Data Convertor Pro software. Finally, post processing is accomplished using a custom MATLAB script, which scales, filters, performs the frequency domain conversion and displays the results. See Figure 4–5 for a picture of the complete system.

4.4 Detailed System Operation

The overall system is a synchronous impulse radar. System synchronization is realized by a 10 MHz reference oscillator from the Tektronix AFG3102 and associating this reference with the LMK_CLKIN port (J1) of the ADC. This ensures that when a trigger even occurs that the data is coherent. Next, the trigger out port of the TSW14J56 Data Acquisition Card (DAC), TRIG_OUT_A (J7), is paired with the trigger-in port of the AFG3102. In a like manor, the trigger-out port of the AFG3102 is referenced to the TRIG_IN (J13) on the TSW14J56. The HSDCPro software is then used to invoke a capture sequence. The output trigger from the

49
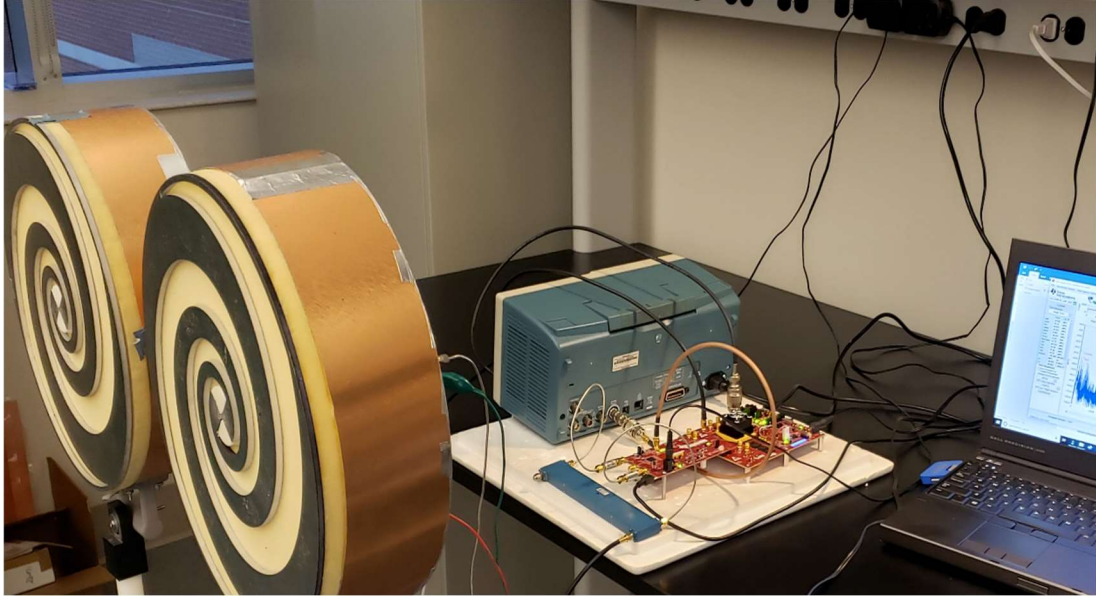
Figure 4–5 Compete System

TSW14J56 causes the AFG3102 to trigger and create the pulse train that is used as the input to create the narrow band pulses. This, in turn, causes the AFG3102 to send an output trigger back to the TSW14J56 to begin a capture sequence. At this point, the data is pulled from the DAC by the HSDCPro software for analysis or exported from the module as a .csv file with magnitude expressed as ADC bits in signed format. For the range profile, the later format was used, and the file was processed by a custom MATLAB script.

Since the user sets the sampling rate and the number of bins (samples) that are obtained, (up to a maximum of 1,073,741,824 samples per channel) a calibration test can be run to factor out the system group delay for accurate ranging measurements. See Figure 4–6 for the configuration GUI. This was done experimentally, and the calibration factor was used for the high-resolution range profile testing. For this system configuration, the delay was 440.8 ns.
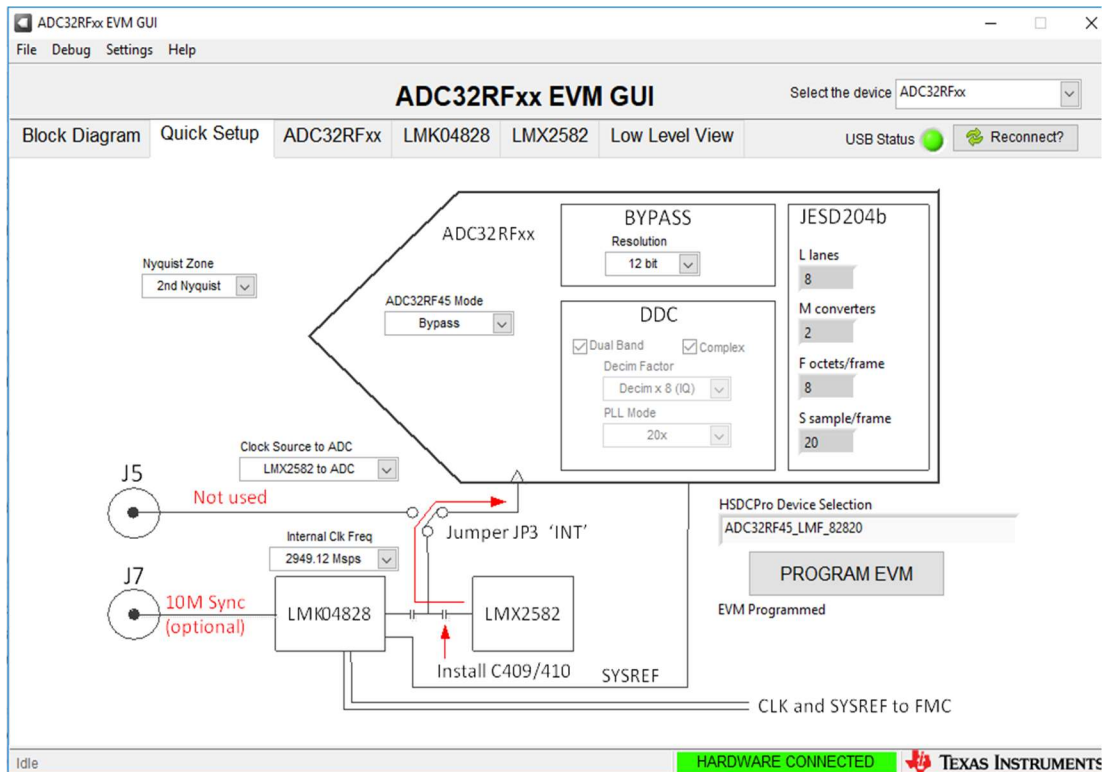
Figure 4–6 ADC Configuration GUI

The amplifier blocks, Mini-Circuits ZX60-2534MA+, are selected based on the noise figure, gain and frequency range, which are 2.6 dB, ~37.5 dB and 0.5-2.5 GHz respectively. Two matched amplifiers are used to create a symmetrical Tx/Rx path.

The Krytar 90° Hybrid Coupler is used to create the phase shift needed for the I and Q signals. The operating frequency range for the device is 0.5-7.0 GHz with only a 0.4 dB amplitude imbalance and 5° phase imbalance over the entire band. It is found through measurement that the values over the 0.75-1.25GHz range are less than 0.5 dB and 1°.

The antialiasing filters, Mini-Circuits VLF-1200, are applied to both ADC inputs. These devices have a passband of DC-1.2 GHz (less than 1 dB of insertion loss)

and a stopband of 1.865-6.2 GHz with 20 dB (minimum) loss. These devices are critical for preventing aliased data from contaminating the received signals. Particularly since the testing environment is not in a EMC chamber and a great deal of unwanted spectral content above the Nyquist range of the ADC is present.

The pulse generator circuit is adopted from previous work from the University of Tennessee. See Figure 4–7. It creates a sub-nanosecond 1 V mono-pulse from a 5 Vpp 10 MHz sine wave from the AFG3102.
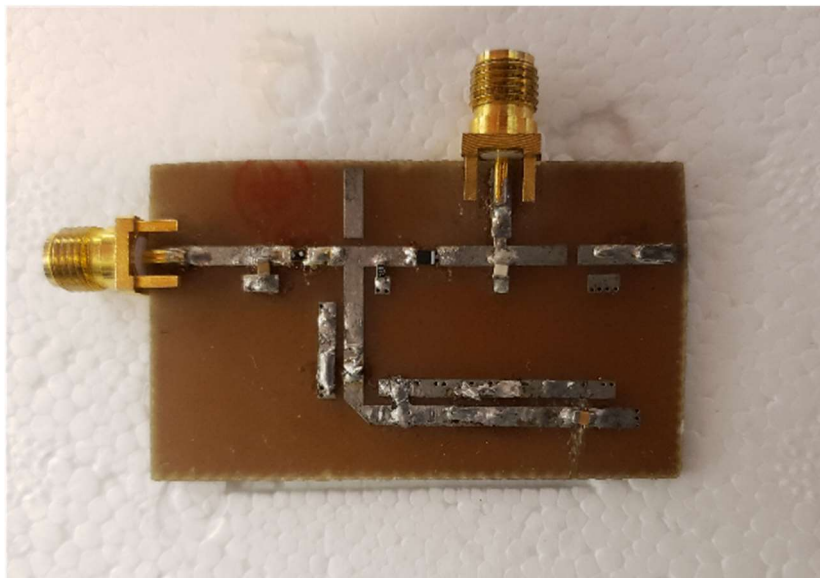
Figure 4–7 Pulse Generator Circuit

4.5 Design Validation

To validate the performance, a high-resolution range profile (HRRP) experiment is conducted, and the results compared to a previously development equivalent time sampled (ETS) impulse radar system.

The ETS system and data used as a reference were originally published in [53]. The test setup is shown in Figure 4–8.
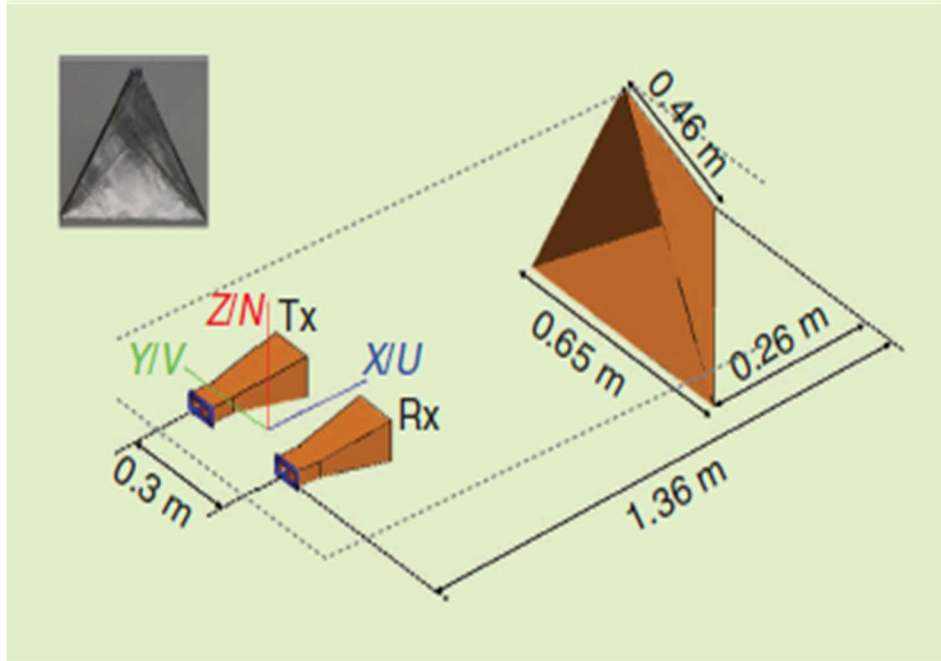
Figure 4–8 Test Configuration from original ETS system

For the new test configuration, the previous test setup is recreated as much as possible. However, the following variations should be noted. The distance separating the antennas is increased from 0.3 m to 0.35 m as the physical dimensions of the spiral antennas prevented closer proximity. Also, the antennas used are circularly polarized as opposed to the linearly polarized double ridge horn antennas that were used in the referenced work. In addition, the test measurements were conducted outside of an anechoic chamber as the frequency range of the system is below the cut-off of the available chamber. Figure 4–9 provides a photo depicting the new test setup. While no vertical distances were specified in the reference work, the center of the antennas and the target reflector were used.

The ETS HRRP obtained from [53] can be seen in Figure 4–10.

Figure 4–9 HRRP Test Setup for RFDS radar
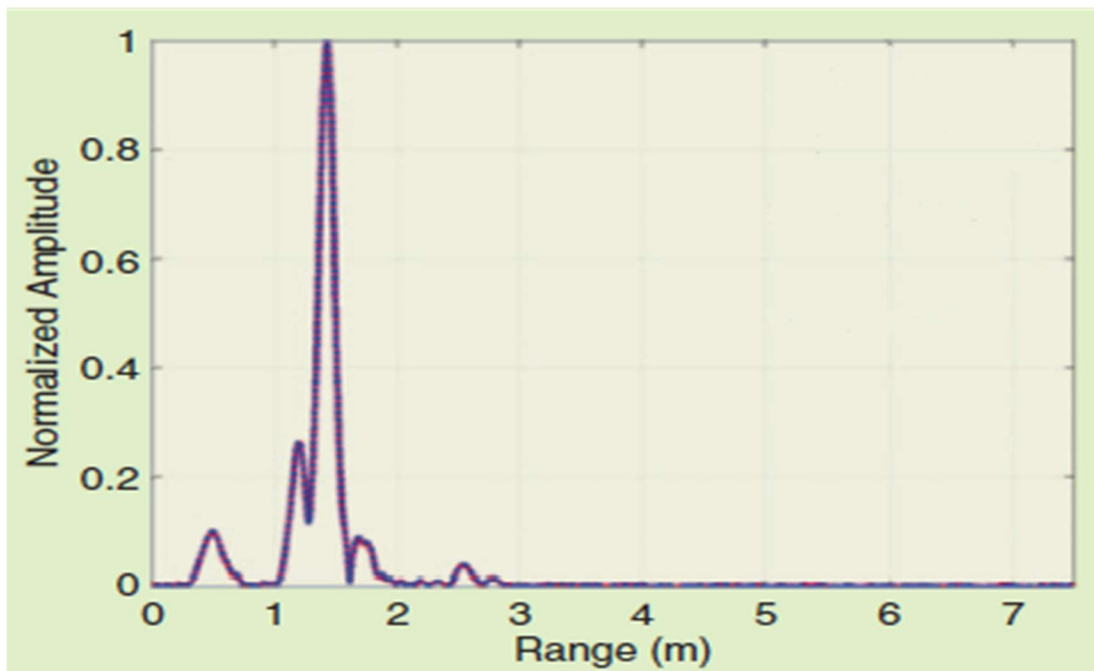
Figure 4–10 Normalized HRRP Results from ETS impulse radar

When we view and contrast this graph to the new system HRRP, as shown in Figure 4–11, additional details of the system performance can be seen.

By comparison between the ETS system and the direct sampling one, it can be seen that the range profiles produce very similar results. Of primary note, the two systems show a strong return at 1.36 m. The graph found in Figure 4–11 is constructed by using a single data capture of 4096 elements (bins) with a sampling rate of 2.94912 GHz which produces a view of ~1.4 µs. The pulse repetition rate (PRT) is 9.8304 MHz. For the creation of the HRRP, a 5-pulse pulse-train was used. The combination of PRT and sampling rate creates a 300 bin / pulse resolution. Figure 4–12, Figure 4–13 and Figure 4–14 show the I, Q and normalized time domain equivalent for the pulse signal, respectively.
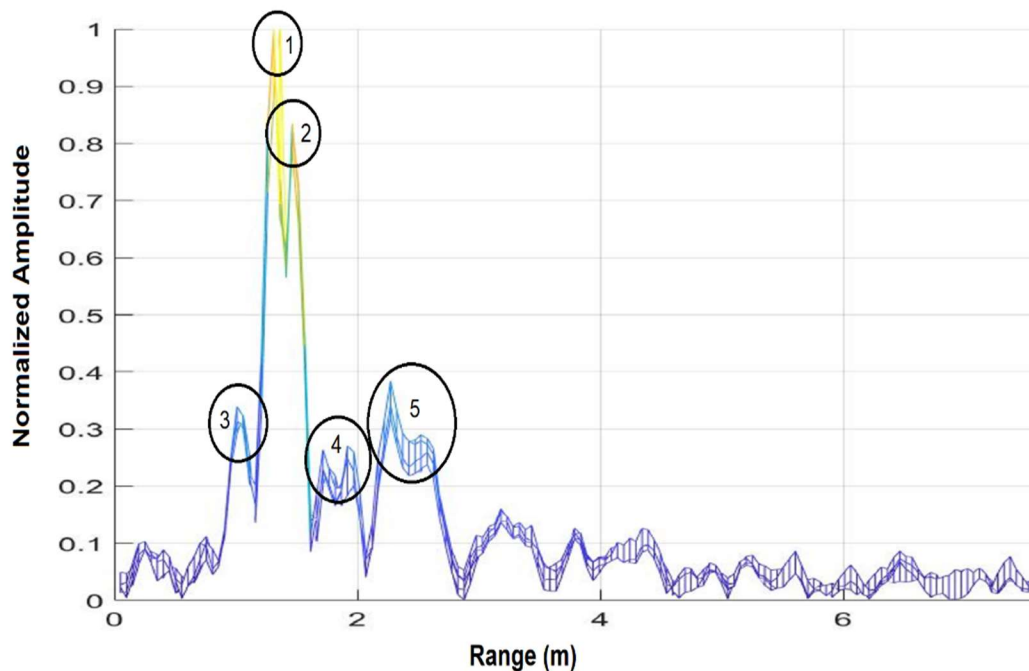
Figure 4–11 Normalized HRRP from RF DS Impulse Radar Depicting Target Features. (1) Horizontal Vertexes, (2) Vertical Vertex, (3) Leading Edge, (4) Middle Pedestal, (5) Lower Pedestal
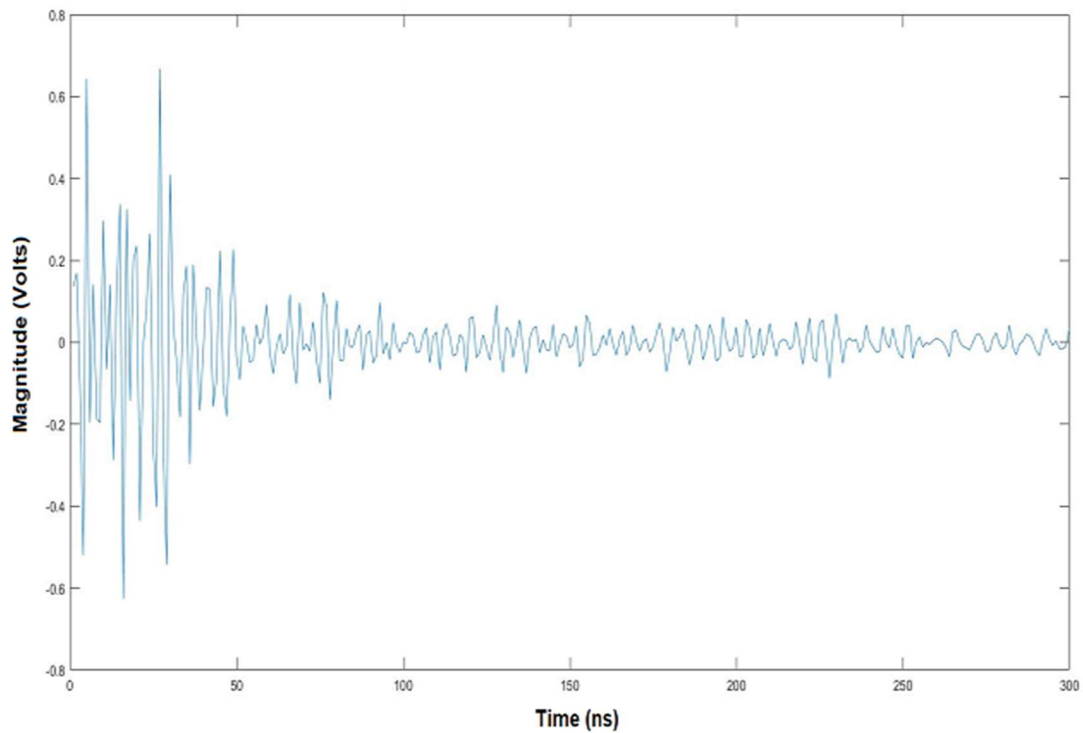
Figure 4–12 HRRP Discrete Time Domain Single Pulse (Frame), I Signal
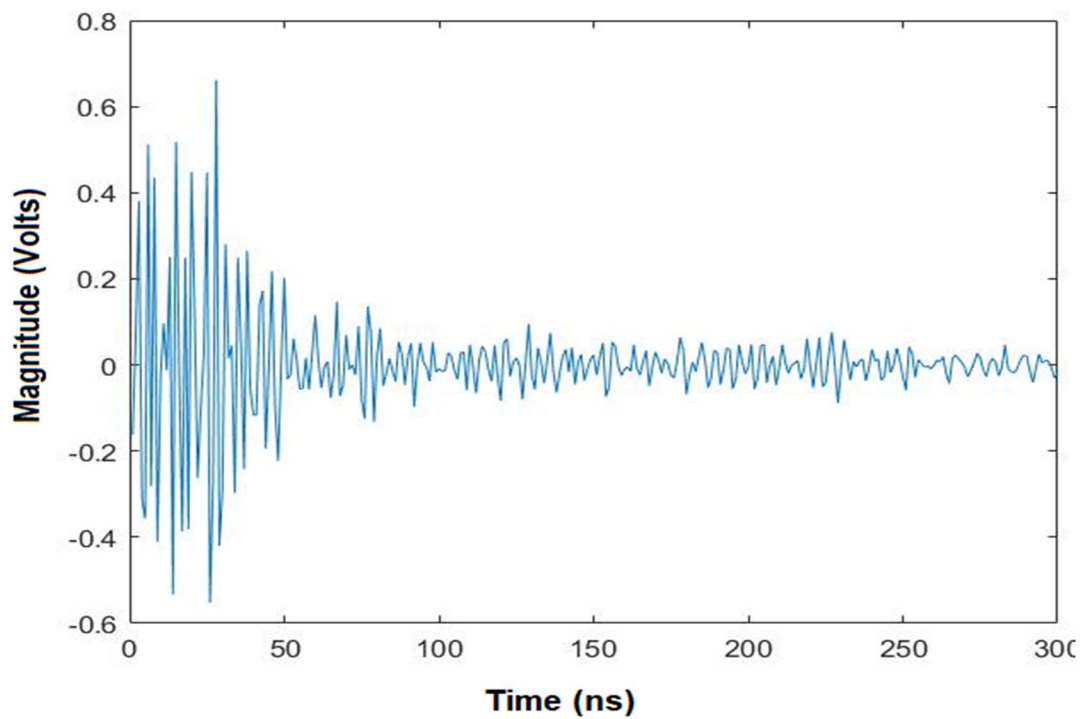
Figure 4–13 HRRP Discrete Time Domain Single Pulse (Frame), Q Signal

56
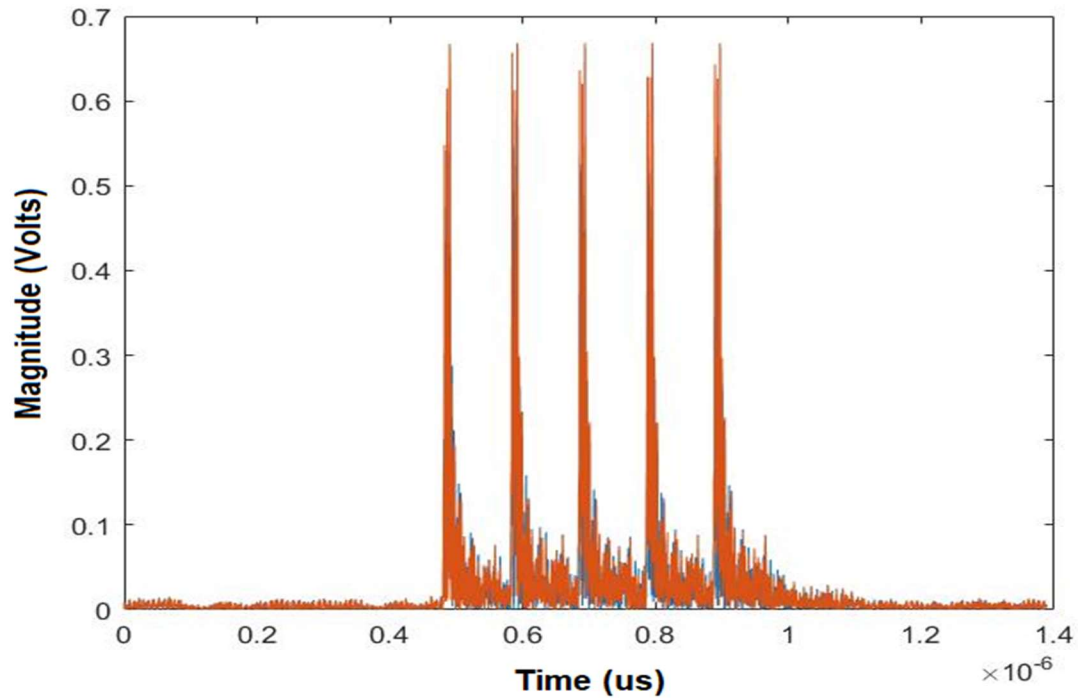
Figure 4–14 Normalized Time Domain Scene

4.6 Conclusion

As provided from [54], Table 4-3 and Table 4-4 compare and contrast the overall specification of the two systems. It is evident from these tables that the two systems are similar. However, the direct sampled impulse radar as fabricated and tested shows higher resolution with less system hardware complexity than the ETS system. In addition, the post processing requirements and amount of data are significantly less. Finally, we are also capable of making measurements in near real-time with dynamic scenes (situations in which the target is moving) with the impulse radar system, which is impossible with the techniques used for the ETS system.

Table 4-3 Isolation Requirements between Tx and Rx for ETS and RF DS Systems

Parameters	ETS Values	RF DS Values
Transmitter Total Power (dBm)	25	18
Rx 1dB Compression Point (dBm)	0	18
Required Tx-Rx Isolation (dB)	25	36

Table 4-4 Dynamic Range Analysis of the ETS and RF DS radar

Parameter	ETS Value	RF DS Value
Rx Thermal Noise Floor (dBm/Hz)	-174	-174
Receiver Bandwidth (GHz)	3	3.2
Receiver Thermal Noise Floor (dBm)	-79	-79
Receiver Noise Figure (dB)	8	3
Receiver Noise Floor (dBm)	-71	--76
Required SNR (dB)	6	6
Receiver Sensitivity (dBm)	-65	--70
Rx 1dB Compression Point (dBm)	0	18
Receiver Dynamic Range (dB)	65	88

CHAPTER 5:

CONCLUSION AND FUTURE WORK

5.1 Introduction

In this chapter the conclusion of the direct sampled impulse radar will be discussed, and future work will be explored.

5.2 Conclusions

The goal of this thesis project is to create an ultra-wideband direct sampling radar system that is suitable for impulse radar applications and detection of subsurface objects. The system has true ultra-wideband capabilities from 750-1250 MHz with excellent overall system characteristics that include match, gain, SNR and range resolution. In addition, the antennas, while physically large to accommodate the lower frequency range, are quite robust and capable of being used without fear of damage.

5.3 Future Work

During the development of the current system, there were many revelations concerning the system capabilities as well as restrictions and limitations. After exploring the regulatory restrictions for instance, it became obvious that additional work and cooperation will need to take place with the FCC to realize higher power/penetration systems. Spatial resolution is another area of potential improvement. The systems frequency and bandwidth could be increased by using antennas with higher center frequency and wider bandwidth or a more ambitious approach would be changing to a direct conversion system that would allow a shift

to a higher frequency range to optimize the bandwidth and increase cross-range resolution, minimize regulatory restrictions and spectral congestion.

Finally, many of the data processing elements that have been delegated to an external PC and MATLAB application could be handled by the Intel FPGA on the TSW14J56 that is part of the ADC/DAC development boards. By including the FFT and other signal processing tasks in the FPGA, near real time analysis and imaging could be achieved.

REFERENCES

[1] L. Peters and J. D. Young, Time-Domain Measurements in Electromagnetics, New York, NY: Van Norstrand Reinhold, 1986.

[2] D. L. Moffatt and R. J. Puskar, "A subsurface electromagnetic pulse radar," *Geophysics,* vol. 41, pp. 506-518, 1976.

[3] D. J. Daniels, D. J. Gunton and H. F. Scott, "Introduction to subsurface radar," *Proc. IEE,* Vols. 135, pt. F, no. 4, pp. 278-320, 1988.

[4] L. Peters, J. J. Daniels and J. D. Young, "Ground penetrating radar as a subsurface environmental sensing tool," *IEEE,* vol. 82, pp. 1802-1822, 1994.

[5] R. P. King and C. W. Harrision, Jr., "The transmission of electromagnetic waves and pulses into the earth," *Applied Physics,* vol. 39, pp. 4444-4452, 1968.

[6] G. S. Smith and W. R. Scott, Jr., "A scale model for studying ground penetrating radars," *IEEE Geoscience Remote Sensing,* vol. 27, pp. 358-363, 1989.

[7] C. Liu and C. Shen, "Numerical simulatin of subsurface radar for detecting buried pipes," *IEEE Transactions on Geoscience Remote Sensing,* vol. 29, pp. 795-798, 1991.

[8] J. M. Bourgeois and G. S. Smith, "A fully three-dimensional simulation of a ground-penetrating radar: FDTD theory compared with experiment," *IEEE Transactions on Geoscience Remote Sensing,* vol. 34, pp. 36-44, 1996.

[9]   K. A. Michalski and D. Zheng, "Electromagnetic scattering and radiation by surfaces of arbitrary shape in layered media, Part I and II," *IEEE Transactions on Antenna Propagationi,* vol. 38, pp. 335-352, 1990.

[10] S. Macintosh, "Introduction to GPR," in *Phytosequestration Workshop*, Chicago, IL, 2015.

[11] "Chapter 20: Analog to Digital Convesion," Analog Devices, 5 9 2013. [Online]. Available: https://wiki.analog.com/university/courses/electronics/text/chapter-20. [Accessed 6 10 2018].

[12] J. H. Reed, Software Radio: A Modern Approach to Radio Engineering, Saddle River, NJ: Pearson Education, Inc., 2002.

[13] R. H. Walden, "Analog-to-digital converter survey and analysis," *IEEE Journal of Selcted Areas of Communications,* vol. 17, no. 4, pp. 539-550, 1999.

[14] P. R. Gray, P. J. Hurst and S. H. Lewis, Analysis and Design of Analog Integrated Circuit design, 4th ed., Hoboken, NJ: Wiley, 2001.

[15] M. Shinagawa, Y. Akazawa and T. Wakimoto, "Jitter analysis of high-speed sampling systems," *IEE Journal of Solid-State Circuits,* vol. 25, no. 1, pp. 220-224, 1990.

[16] K. Uyttenhove and S. J. Steyaert, "Speed-power-accuracy tradeoff in high-speed CMOS ADCs," *IEEE Transactions circuits Systems II,* vol. 49, no. 4, pp. 280-287, 2002.

[17] R. Lyons, Understanding Digital Singal Processing, 3rd Ed, Ann Arbor: Prentice Hall, 2011.

[18] P. B. Kenington and L. Astier, "Power consumption of A/D converters for software radio applications," *IEEE Transactions on Vehicle Technology,* vol. 49, no. 2, pp. 643-650, 2000.

[19] P. B. Kenington and L. Astier, "Power consumption of A/D converters for software radio applications," *IEEE Transactions on Vehicle Technology,* vol. 49, no. 2, pp. 643-650, 2000.

[20] R. Gomez, "Theoretical Comparison of Direct-Sampling Versus Heterodyne RF Receivers," *IEEE Transactions on Circuits and Systems,* vol. 63, no. 8, pp. 1276-1282, 2016.

[21] V. J. Arkensteijn, E. A. Klumperink and B. Nauta, "Jitter requiremenets of the sampling clock in software radio receivers," *IEEE Transactions Circuits Systems II,* vol. 53, no. 2, pp. 90-94, 2006.

[22] B. van Liempd, "A 0.9 V 0.4-6 GHz harmonic recombination SDR receiver in 28 nm CMOS with HR3/HR5 and IIP2 calibration," *IEEE Journal Solid-State Circuits,* vol. 49, no. 8, pp. 1815-1826, 2014.

[23] Y. C. Choi, Y. J. Seong, S. K. Lee, M. Velazquez Lopez and H. J. Yoo, "Multi-standar hybrid PLL with low phase-noise charasteristcs for GSM/EDGE and LTE applications," *IEEE Transactions Microwave Theory Technology,* vol. 63, no. 10, pp. 3254-3264, 2015.

[24] T. Georgantas, "9.1 A 13mm^2 40 nm multiband GSM/EDGE/HSPA+/TD SCDMA/LTE transceivers," in *IEEE International Solid-State Circuits Conference (ISSCC)*, 2015.

[25] Y. He and Y. Akizuki, "FDTD analysis of a planar spiral antennas for the ground penetrating radar," in *URSI International Symposium on Electromagnetic Theory*, Berlin, 2010.

[26] G. Klysz, J. P. Balayssac, S. Laurens and X. Ferrieres, "Numerical FDTD simulation of the direct wave propagation of a GPR coupled antenna," in *10th International Conference on Ground Penetrating Radar*, Delt, Netherlands, 2004.

[27] D. Valderas, J. I. Sancho, D. Puente, C. Ling and X. Chen, Ultrawideband Antennas Design and Applications, London, UK: Imperial College Press, 2011.

[28] R. H. Rumsey, Frquency Independent Antennas, New York: Academic Press, 1966.

[29] I. Hertl and M. Strycek, "UWB Antennas for Ground Penetrating Radar Applicatioin".

[30] J. Thaysen, K. B. Jakobsen and J. Appel-Hansen, "Ultra wideband coplanar waveguide fed spiral antenna for humanitarian demining," in *30th European Microwave Conference*, Paris, France, 2000.

[31] A. Casas, V. Pinto and L. Rivero, "Fundamentals of ground penetrating radar in environmental and engineering applications," *Annals of Geophysics,* vol. 43, no. 6, pp. 1091-1103, 2000.

[32] J. Thaysen, K. B. Jakobsen and J. Appel-Hansen, "Circular polarized stepped frequency ground-penetrating radar for humanitarian demining," in *Proceedings of SPIE 4394, Detection and Remediation Technologies for Mines and Minelike Targets VI*, 2001.

[33] R. Kazemi, "Development of a logarithmic spiral antenna in UWB GPR for humanitarian demining," *Electromagnetics,* vol. 38, no. 6, pp. 366-379, 22 June 2018.

[34] J. Thaysen, J. K. Jakobsen and H. R. Lenler-Eriksen, "Wideband cavity backed spiral antenna for stepped frequency ground penetrating radar," in *IEEE International Symposium on Antennas and Propagation*, Washington DC, USA, 2005.

[35] Y. Mushiake, "Self-complementary antennas," *IEEE Antennas and Propagation Magazine,* vol. 34, no. 6, pp. 23-29, 1992.

[36] J. D. Dyson, "The equiangular spiral antenna," *IRE Transactions on Antennas and Propagation,* vol. 7, no. 2, pp. 181-187, 1959.

[37] P. Piksa and M. Mazanek, "A Self-Complementary 1.2 to 40 GHz Spiral Antenna with Impedance Matching," *Radioengineering,* vol. 15, no. 3, pp. 15-19, 2006.

[38] C. Seong and D. C. Park, "Design of cavity-backed spiral antennas," in *5th Global Symposium on Millimeter Waves (GSMM)*, Harbin, China, 2012.

[39] J. Thaysen, "Logarithmic spiral antenna and feed network for application to humanitarian deming," Masters Thesis, Technical University of Denmark, 2000.

[40] H. G. Schantz, "Dispersion and UWB antennas," in *International Workshop on Ultra Wideband Systems*, Kyoto, Japan, 2004.

[41] C. A. Balanis, Antenna Theory: Analysis and design, 3rd Ed., Hoboken, NJ, USA: Wiley Interscience, 2005.

[42] J. D. Daniels, "Surface-Penetrating Radar," in *IEEE*, London, UK, 1996.

[43] A. G. Yarovoy, A. D. Schukin, I. V. Kaploun and L. P. Ligthart, "The dielectric wedge antenna," *IEEE Transactions on Antenas and Propagation,* vol. 50, no. 10, pp. 1460-72, 2002.

[44] E. M. Johansson and J. E. Mast, "Three-dimensional ground penetrating radar imaging using synthetic aperture time-domain focusing," in *Proceedings SPIE 2275, Advanced Microwave and Millimeter-Wave Detectors*, San Diego, CA, 1994.

[45] S. Vitebskiy, L. Carin, M. A. Ressler and F. H. Le, "Ultra-Wideband, Short-Pulse Ground-Penetrating Radar: Simulation and Measurement," *IEEE Transactions on Geoscience and Remote Sensing,* vol. 35, no. 3, pp. 762-772, 1997.

[46] S. Lambot, L. Weihermuller, J. A. Huisman, H. Vereecken, M. Vanclooster and E. C. Slob, "Analysis of air-launched ground-penetrating radar techniques to measure the soil surface water content," *Water Resources Research,* vol. 42, pp. 1-12, 2006.

[47] A. B. Suksmono, E. Bharata, A. A. Lestari, A. G. Yarovoy and L. P. Ligthart, "Compressive Stepped-Frequency Continuos-Wave Ground-Penetrating Radar," *IEEE Geoscience and Remote Sensing Letters,* vol. 7, no. 4, pp. 665-669, 2010.

[48] A. Ahmed, Y. Zhang, D. Burns, D. Huston and T. Xia, "Design of UWB Antenna for Air-Coupled Impulse Ground-Penetrating Radar".

[49] L. Miccinesi, N. Rojhani and M. Pieraccini, "Compressive Sensing for No-contact 3D Ground Penetrating Radar," University of Florence, Firenze, Italy, 2018.

[50] D. J. Daniels, Ground Penetrating Radar, 2nd Edition, London, UK: Institution of Electrical Engineers, 2004.

[51] B. R. Mahafza, Radar Systems Analysis and Design Using MATLAB, 3rd Ed., Boca Raton, FL: CRC Press, 2013.

[52] C. Zhang, "Reconfigurable Pico-Pulse Generator for UWB Applications," *IEEE,* vol. 6, no. 5, pp. 407-410, 2006.

[53] H. Wang, V. Dang, L. Ren, Q. Liu, L. Ren, E. Mao, O. Kilic and A. Fathy, "An Elegeant Solution," *IEEE Microwave Magazine,* pp. 53-63, July 2016.

[54] Y. Wang, "UWB Pulse Radar for Human Imaging and Doppler Detection Applications," University of Tenessee, Knxoville, 2012.

[55] T. A. Milligan, Modern Antenna Design, Hoboken, NJ: Wiley-IEEE Press, 2005.

[56] P. T. P. Klenk, "Developing Ground-Penetrating Radar for Quantitative Soil Hydrology," Ruperto-Carola University, Heidelberg, Germany, 2012.

[57] J. C. Maxwell, "A treatise on electricity and magnetism," Clarendon Press, Oxford, UK, 1973.

[58] P. V. Sharma, Environmental and engineering geophysics, Cambridge, UK: Cambridge University Press, 2002.

[59] A. Annan, GPR Methods for Hydrogeological Studies. In: rubin Y., Hubbard S.S. (eds) Hyrogeophsics. Water Science and Technology Library, vol 50, Springer, The Netherlands: Springer, Dordrecht, 2005.

[60] J. Jackson, Classical Electrodynamics, John Wiley & Sons, 1998.

[61] A. Shivola, Electromagnetic Mixing Formulas and Applications, London, UK: The Institution of Electrical Engineers, 1999.

[62] R. Buchner, J. Barthel and J. Stauber, "The dielectric relaxation of water between 0C and 35C," *Chemical Physics Letters,* vol. 306, no. 1-2, pp. 57-63, June 1999.

[63] R. C. Weast, M. J. Astle and W. H. Beyer, CRC Handbook of Chemistry and Physics, Boca Raton, FL: CRC Press, Inc., 1989.

[64] D. A. Noon, "Stepped-Frequency Radar Design and Signal Processing Enhances Groound Penetrating Radar Performance," The University of Queensland and Cooperative Research Centre for Sensor Signal and Information Processing, Queensland, Australia, 1996.

[65] J. Thaysen, K. B. Jakobsen and J. Appel-Hansen, "Numerical and experimental investigation of a coplanar waveguide-fed spiral antenna," in *24th QMW Antenna Symposium*, London, UK, 2000.

[66] J. D. Dyson, "The unidirectional equiangular spiral antenna," *IRE Transactions on Antennas and Propagation,* vol. 7, no. 4, pp. 329-334, 1959.

[67] R. G. Corzine and J. A. Mosko, Four Arm Spiral Antennas, Boston: Artech House, 1990.

[68] G. A. Deschamps, "Impedance properties of complementary multi-terminal planar structures," *IRE Transactions on Antennas and Propagation,* Vols. AP-7, pp. S371-378, 1959.

[69] J. A. Huffman and T. Cencich, "Modal impedances of planar, non-complmentary, N-fold symmetric antenna structures," *IEEE Antennas and Propagation Magazine,* February 2005.

[70] B. Le, T. W. Rondeau, J. H. Reed and C. W. Bostian, "Analog-to-Digital Converters," *IEEE Signal Processing Magazine,* pp. 69-77, 11 2005.

[71] T. K. Callaway and E. E. Swartzlander, "Optimizing arithmetic elements for signal processing," in *Workshop VLSA Signal Processing V*, 1992.

[72] A. Stillmaker, Z. Xiao and B. Baas, "Toward more accurate scaling estimates of CMOS circuits form 180 nm to 22 nm," University of California, Davis, Davis, CA, USA, 2011.

[73] IEEE, *686-1990 - IEEE Standard for Radar Definitions,* IEEE, 1990.

[74] M. I. Skolnik, Introduction to Radar Systems, New York, NY: McGraw-Hill, 1962.

[75] J. MacDonald, J. Loockwood, T. Altshuler, T. Broach, L. Carin, R. Harmon, C. Rappaport, W. Scott and R. Weaver, Alternatives for Landmine Detection, Santa Monica, CA: RAND, 2003.

[76] M. Acheroy, "Status of sensor technology for clse-in and remote detection of anti-personnel mines," *Near Surface Geophysics,* no. 5, pp. 45-55, 2007.

VITA

Matthew Richardson was born in 1972 in Bellaire, Ohio. His parents John and Barbara Richardson had three children; John, Matthew and Adam. He obtained his Bachelor of Science in electrical engineering in 1998 from the University of North Carolina at Charlotte. He worked as an electrical engineer in the greater North Carolina area for over 15 years at which point he moved to Tennessee in 2013. He began a Master of Science in electrical engineering in 2015 while working full time. He completed his degree in 2018. Matthew, along with his wife Indira, and son Quinn, currently reside in Oak Ridge Tennessee.